

Effect of spin in binary neutron star mergers

Beyhan Karakas,¹* Rahime Matur,²† Maximilian Ruffert³

¹*Mevlana Mah. 1735 Sok. No:3 Kat:2 Bornova. Izmir, 35050, Turkey*

²*Mathematical Sciences and STAG Research Centre, University of Southampton, Southampton SO17 1BJ, UK*

³*School of Mathematics and Maxwell Institute, University of Edinburgh, Edinburgh EH9 3FD, UK*

Accepted XXX. Received YYY; in original form ZZZ

ABSTRACT

We investigate the effect of spin on equal and unequal mass binary neutron star mergers using finite-temperature, composition-dependent Hempel-Schaffner-Bielich (SFHo) equation of state, via 3+1 general relativistic hydrodynamics simulations which take into account neutrino emission and absorption. Equal mass cases that have a mass of $M_{1,2} = 1.27, 1.52$ and $2.05M_{\odot}$, result in a supramassive neutron star, a delayed, and a prompt collapse to a black hole, respectively. For all cases, we analyse the effect of initial spin on dynamics, on the structure of the final remnant, its spin evolution, the amount and composition of the ejected matter, gravitational waves, neutrino energy and luminosities, and disc masses. We show that in equal mass binary neutron star mergers, the ejected mass could reach $\sim 0.085M_{\odot}$ for highly aligned-spins ($\chi = 0.67$). The black hole which results from such highly spinning, high-mass binary neutron star merger reaches a dimensionless spin of 0.92; this is the highest spin reached in binary neutron star mergers, to date.

Key words: stars: neutron – stars: rotation – neutrinos – gravitational waves – hydrodynamics

1 INTRODUCTION

The detection of gravitational wave event GW170817 [Abbott et al. \(2017a\)](#) by the Advanced LIGO [The LIGO Scientific Collaboration \(2015\)](#) and Advanced Virgo [Acernese et al. \(2015\)](#) detectors was found to correspond to the inspiral part of a binary neutron star (BNS) merger. The associated electromagnetic counterpart, associated to the short Gamma-Ray Burst (sGRB) event GRB 170817A, which was observed by The Fermi Gamma-Ray Burst Monitor [Abbott et al. \(2017b\)](#), happened ~ 1.7 s later. This event both questioned a wide range of nuclear and astrophysical theories and showed the long-anticipated link between BNS mergers and sGRBs [Eichler et al. \(1989\)](#); [Piran \(1992\)](#); [Ruffert et al. \(1995, 1997\)](#); [Ruffert & Janka \(2001\)](#), [Abbott et al. \(2017b\)](#). It constrained individual spins, and constrained (and ruled out) very soft equations of state (EOSs) ($M_{max} < 1.97M_{\odot}$) [The LIGO Scientific Collaboration and the Virgo Collaboration et al. \(2018\)](#); [Abbott et al. \(2019a\)](#). It also showed the contribution of BNS mergers to r-process nucleosynthesis and the kilonova [Kasen et al. \(2017\)](#); [Smartt et al. \(2017\)](#); [Pian et al. \(2017\)](#); [Troja et al. \(2017\)](#); [Hallinan et al. \(2017\)](#), the robustness of the general theory of relativity in the strong gravity regime [Abbott et al. \(2019b\)](#) and placed constraints on alternative theories of gravity [Sakstein & Jain \(2017\)](#); [Baker et al. \(2017\)](#). The current detectors are only sensitive to the inspiral period of these events, which allows to measure three important parameters of the system, namely chirp mass [Kafka \(1988\)](#); [Finn & Chernoff \(1993\)](#); [Cutler et al. \(1993\)](#); [Cutler & Flanagan \(1994\)](#), effective spin χ and tidal deformability λ , [Hinderer \(2008\)](#); [Flanagan & Hinderer \(2008\)](#); [Hinderer et al. \(2010\)](#);

[Read et al. \(2013\)](#); [Abbott et al. \(2017b\)](#). Assuming high spin rates, both aligned with the orbital angular momentum, ($|\chi| \leq 0.89$), the chirp mass, effective spin and dimensionless tidal deformability parameter of the binary (Λ) were measured for the GW170817 event to be $M_{chirp} = 1.188^{+0.004}_{-0.002} M_{\odot}$, $\chi \in (0.0, 0.09)$, and $\Lambda < 800$ (for 90 per cent credibility level) [Abbott et al. \(2017a\)](#), respectively. Measurement of the tidal deformability parameter is the key to extract the EOS information from gravitational waves.

The GW190425 event [Abbott et al. \(2020\)](#) was found to correspond to the inspiral part of the BNS merger. Assuming high spins of the inspiralling neutron stars, the effective spin was measured to be $\chi = 0.058^{+0.11}_{-0.05}$. No electromagnetic (EM) counterpart was detected for this event.

Creating spinning BNS initial data (ID) was first discussed by [Marronetti & Shapiro \(2003\)](#) who use the conformal thin-sandwich (CTS) method. [Tichy \(2006, 2009a,b, 2011, 2012\)](#); [Tichy et al. \(2019\)](#), make use of the CTS method and split the fluid velocity into irrotational and rotational parts, the so-called constant rotational velocity (CRV) approach, to create BNS ID. [Tsatsin & Marronetti \(2013\)](#) use the Rapidly Rotating Neutron Star (RNS) code to create BNS ID by mapping two isolated solutions into a single frame. [Tacik et al. \(2015\)](#) use the extended-CTS (xCTS) method and the CRV approach of Tichy to create BNS ID. [Papenfort et al. \(2021\)](#) use Fuka which is an extension of the Kadath library [Grandclement \(2010\)](#) and the xCTS method to create BNS ID.

Even though our understanding of the BNS system has evolved from searching for the possibility of forming BHs in the inspiral part of a BNS merger [Wilson & Mathews \(1995\)](#) to studying the realistic neutrino absorption/emission of spinning, magnetized BNS merger in full general relativity, current simulations still have many simplifications which are hard to remove.

* E-mail: beyhannkarakas@gmail.com

† E-mail: r.matur@soton.ac.uk

We focus on the effect of varying spin on mergers of equal and unequal mass BNS in quasi-circular orbit. The centre-to-centre separation is 40km. We use the finite-temperature, composition-dependent Hempel-Schaffner-Bielich (SFHo) EOS by [Steiner et al. \(2013\)](#), taking into account neutrino emission & absorption through 3+1 general relativistic hydrodynamic (GRHD) simulations. The properties of the initial data (ID) are given in Table 1.

We investigate effective spin parameters with values of $\chi = -0.65, -0.4, -0.2, 0, +0.2, +0.4, +0.67$, where the negative (positive) sign denotes having spin angular momentum anti-aligned (aligned) with the orbital angular momentum, respectively. In these configurations, there are three case which have zero effective spin and are denoted as $\chi = 0[1], 0[2], 0[3]$. They correspond to having individual spins of $\chi_{1,2} = 0, \pm 0.4$ and ± 0.65 , respectively.

The paper is organized as follows: in section 2, we describe the setup for the initial data and the numerical method, results are given in section 3, the conclusion follows in section 4 and an appendix A ends this paper. We use geometrized units, where ($G = c = 1$), unless specified otherwise.

2 NUMERICAL SETUP

All BNS ID are created using the Fuka branch of the Kadath library [Grandclement \(2010\)](#); [Papenfort et al. \(2021\)](#). We present the values of the ID in Table 1.

GRHD evolution is performed by `WhiskyTHC` [Radice & Rezzolla \(2012\)](#); [Radice et al. \(2014a,b\)](#); [Radice et al. \(2015\)](#). This was built on top of `Cactus` [Allen et al. \(1999\)](#); [Goodale et al. \(2003\)](#); `Cactus developers (2023a,b)` and uses the `Carpet` adaptive mesh refinement (AMR) driver [Schnetter et al. \(2004\)](#) of `Cactus`. `WhiskyTHC` is a fourth-order finite difference/finite volume High-Resolution Shock-Capturing (HRSC) code that implements the Valencia formulation [Banyuls et al. \(1997\)](#) of GRHD. It models the neutron stars as perfect fluids with the energy-momentum tensor given as [Radice & Rezzolla \(2012\)](#); [Radice et al. \(2014a,b\)](#); [Radice et al. \(2015\)](#):

$$T_h^{ab} = \rho h u^a u^b + p g^{ab} \quad (1)$$

where a, b run from 0 to 3, and ρ, h, p, u^a and g^{ab} are the rest-mass density, enthalpy $h = 1 + \epsilon + p/\rho$, with ϵ the specific internal energy, the pressure, fluid 4-velocity, metric tensor, respectively. T_h^{ab} represents the energy-momentum tensor for pure hydrodynamics. For our systems, the atmosphere density and temperature are set to $\rho = 6.176 \times 10^3 \text{ g cm}^{-3}$ and $T = 0.02 \text{ MeV}$.

The conservation of total energy-momentum, including neutrinos, is given by $\nabla_b T_{rad}^{ab} = Q u^b$, where Q is the net energy deposition rate due to the absorption and emission of the neutrinos [Radice et al. \(2018\)](#).

We use the finite-volume HRSC method which employs a 5th order monotonicity-preserving scheme (MP5) [Suresh & Huynh \(1997\)](#) for reconstruction and the Harten-Lax-van Leer-Einfeldt (HLLE) Riemann solver [Einfeldt \(1988\)](#) for flux calculation.

Neutrinos are taken into account with the zero moment scheme M0 [Radice et al. \(2016b\)](#), which is available in `WhiskyTHC`. It tracks electron, ν_e , anti-electron, $\bar{\nu}_e$ and heavy lepton, ν_μ , neutrinos, which are composed of the muon and tau neutrino & anti-neutrinos. Neutrinos are split into trapped and free-streaming; they are evolved with a leakage scheme and are distributed radially by the M0 scheme (see [Radice et al. \(2016b\)](#) for the detailed explanation of the neutrino treatment). The average energy of free-streaming neutrinos is calculated on a uniform spherical grid with radius $\sim 756 \text{ km}$ and a grid with resolution $(r, \theta, \phi) = (3096, 32, 64)$, using 2048 rays.

We use the finite-temperature, composition-dependent SFHo EOS, which is soft and fully hadronic. It is available on [Stellarcollapse \(2017\)](#), [O'Connor & Ott \(2010\)](#).

Spacetime evolution is performed with `CTGamma` [Pollney et al. \(2011\)](#), which is based on the publicly available software platform `Einstein Toolkit` [Löffler et al. \(2012\)](#); [Zilhão & Löffler \(2013\)](#); [Babiuc-Hamilton et al. \(2019\)](#); [Zlochower et al. \(2022\)](#); [The Einstein Toolkit \(2024\)](#). We use the constraint damping z4c formulation by [Bernuzzi & Hilditch \(2010\)](#), which is used within `CTGamma`, with moving puncture gauge conditions.

The comparison of z4c and Baumgarte-Shapiro-Shibata-Nakamura-Oohara-Kojima (BSSNOK) formulations [Nakamura et al. \(1987\)](#); [Shibata & Nakamura \(1995\)](#); [Baumgarte & Shapiro \(1998\)](#) shows that the former has a substantially lower constraint violation, more accurate gravitational wave phase and amplitude ([Weyhausen et al. \(2012\)](#); [Hilditch et al. \(2013\)](#) and references therein).

The coupling between spacetime and GRHD variables is handled by the Method of Lines (MoL). We use the strong stability preserving (SSP) 3rd order Runge-Kutta method [Gottlieb et al. \(2009\)](#); [Radice \(2020\)](#) for time integration. The timestep factor is chosen according to the Courant-Friedrichs-Lewy (CFL) condition to be 0.15.

We use a cell-centred grid structure that extends to $\sim 2835 \text{ km}$ in all three directions except for the lower z axis, where we use reflection symmetry to reduce the computational cost.

We use 7 refinement levels, the finest grid of which has a resolution of $h_1 \sim 221 \text{ m}$ for the case with $M_{1,2} = 1.27 M_\odot$ and $\chi = \pm 0.2 \pm 0.4$, $\chi = 0[1]$ and $\chi = 0[2]$, where $\chi_{1,2} = 0$ and $\chi_1 = -0.4, \chi_2 = 0.4$, respectively. For these configurations, we use the "Mayer" release of the `Einstein Toolkit`.

For all other configurations, we use the "Sophie Kowalevski" release of the `Einstein Toolkit`. When comparing the irrotational models for the two releases, we find the difference to be negligible for our study (which parameters are compared can be seen in section 3.1). The grid structure and domain are the same as in the "Mayer" release, except for an additional refinement level. We use 8 refinement levels for these configurations and performed the simulations with two different resolutions, $h_2 \sim 307 \text{ m}$ and $h_3 \sim 369 \text{ m}$, for the cases with $M_{tot} = 2.55 M_\odot$. For the cases with $M_{tot} = 3.05 M_\odot$ and $4.10 M_\odot$ the initial resolution of $\sim 369 \text{ m}$ was increased to 185 m when the lapse function decreased below $\alpha < 0.25$, using `Trigger` thorn.

For the equal mass models we choose not to take advantage of mirror-symmetry despite its computational desirability. The reason is the ability to resolve the asymmetries which could arise, such as the $m = 1$ one-armed spiral instability. This instability will be discussed in section 3.7.1.

3 RESULTS

All post-processing is performed using `PostCactus` [Kastaun \(2021\)](#) and `Scidata` [Radice \(2023\)](#). Since the simulations with $M_{tot} = 2.55 M_\odot$ are performed with two resolutions, the results given in Tables 1, 2, 3, 4, A1, A2, A3 and A4 that have a " \pm " show the difference between the two resolutions. All figures are created using data from models with resolution $h = 307 \text{ m}$, for $M_{tot} = 2.55 M_\odot$.

The models are named as follows: names shown by " $\chi =$ " correspond to $M_{tot} = 2.55 M_\odot$, while all other models are named according to the total mass, mass ratio (q) and spin (χ). For example, $305q1\chi0$ corresponds to the equal mass and irrotational case with a total mass of $3.05 M_\odot$.

Table 1. The values of the initial data (ID) and of the times to merger. The first 9 models with names " $\chi =$ " all have $M_{tot} = 2.55M_{\odot}$. The values for M_{tot} , $M_{1,2}$ and $M_{1,2}^b$ represent the total mass, the ADM mass of each star in isolation and the baryonic mass of each star. The values for J_0 , f_0 and $\chi_{1,2}$ are the total angular momentum, the initial orbital frequency of the binary and the dimensionless spin parameter of the each star, respectively. The quantity $t - t_{merger}$ shows the difference in inspiral time compared to the equal mass, irrotational case for the same total mass. The equal mass, irrotational cases are marked with * to be easily distinguished. In the inspiral time column, negative (positive) values correspond to the shorter (longer) inspiral time as compared to the equal mass, irrotational case, respectively. The \pm values are the difference between the two resolution models.

Model	$M_{tot} (M_{\odot})$	$M_1 (M_{\odot})$	$M_2 (M_{\odot})$	$M_1^b (M_{\odot})$	$M_2^b (M_{\odot})$	$J_0 (M_{\odot}^2)$	f_0 (Hz)	χ_1	χ_2	$t - t_{merger} (ms)$	
$\chi = 0[1]$	2.5456	1.2728	1.2728	1.3902	1.3902	6.33425	324	0.00	0.00	9.76 ± 0.20	*
$\chi = -0.2$	2.5456	1.2728	1.2728	1.3902	1.3902	5.81142	326	-0.40	0.00	-5.87 ± 0.21	
$\chi = 0.2$	2.5456	1.2728	1.2728	1.3902	1.3902	6.99839	326	0.40	0.00	$+2.05 \pm 0.85$	
$\chi = -0.4$	2.5456	1.2728	1.2728	1.3853	1.3853	5.21892	326	-0.40	-0.40	-7.19 ± 0.20	
$\chi = 0[2]$	2.5456	1.2728	1.2728	1.3902	1.3902	6.43015	326	-0.40	0.40	-5.13 ± 0.22	
$\chi = 0.4$	2.5456	1.2728	1.2728	1.3853	1.3853	7.59055	326	0.40	0.40	$+2.52 \pm 0.42$	
$\chi = -0.65$	2.5456	1.2728	1.2728	1.3701	1.3701	6.38663	326	-0.65	-0.65	-5.13 ± 0.21	
$\chi = 0[3]$	2.5456	1.2728	1.2728	1.3701	1.3701	4.46266	326	-0.65	0.65	-2.76 ± 0.22	
$\chi = 0.67$	2.5456	1.2728	1.2728	1.3695	1.3695	8.39040	326	0.67	0.67	-0.50 ± 0.82	
305q1 χ 0	3.0500	1.5250	1.5250	1.7028	1.7028	8.66939	349	0.00	0.00	7.01	*
305q1 χ 0.4	3.0500	1.5250	1.5250	1.6883	1.6883	10.34024	349	0.40	0.40	+1.25	
305q205 χ 0	3.0500	2.0500	1.0000	2.4215	1.0670	7.64993	348	0.00	0.00	-1.04	
305q205 χ 0.4	3.0500	2.0500	1.0000	2.3391	1.0670	9.95296	348	0.60	0.00	0.37	
41q1 χ 0[1]	4.1000	2.0500	2.0500	2.4215	2.4215	14.43615	385	0.00	0.00	3.55	*
41q1 χ 0[2]	4.1000	2.0500	2.0500	2.3268	2.3268	14.40156	385	-0.65	0.65	-0.65	
41q1 $\chi - 0.65$	4.1000	2.0500	2.0500	2.3268	2.3268	9.71222	385	-0.65	-0.65	-1.71	
41q1 χ 0.67	4.1000	2.0500	2.0500	2.3237	2.3237	19.26407	385	0.67	0.67	+0.82	

The dynamical time is calculated using the peak frequency of $f_{2,2}^{peak}$ mode (in Table 2). The dynamical time corresponds to the period of this frequency ($t_{dyn} = 1/f_{2,2}^{peak}$). We use two comparison times denoted by $t_{dyn,1}$ and $t_{dyn,2}$, where available. The time $t_{dyn,1}$ corresponds to $\sim 19 \times t_{dyn}$ for $M_{tot} = 2.55M_{\odot}$ and is approximately 1.79ms after the BH formation and $\sim 26 \times t_{dyn}$ time for the irrotational and spinning cases for $M_{tot} = 3.05M_{\odot}$, respectively. It corresponds to ~ 3.44 ms after the BH formation for $M_{tot} = 4.10M_{\odot}$. All cases that have $M_{tot} = 2.55M_{\odot}$, except for $\chi = 0[1]$ and $\chi = 0.2$, have $t_{dyn,2}$ at $\sim 34 \times t_{dyn}$ time. For $M_{tot} = 3.05M_{\odot}$, $t_{dyn,2}$ corresponds to approximately 1.79ms after BH formation and $\sim 95 \times t_{dyn}$ time for the equal and unequal mass, spinning cases, respectively.

3.1 Using two versions of the Einstein Toolkit

To show the consistency between the "Mayer" and "Sophie Kowalewski" release of the Einstein Toolkit, see section 1 and section 2 for details, we compared irrotational cases and found the difference in M_{ej} , the mass weighted average electron fraction, $\langle Y_e \rangle$, and velocity, $\langle v \rangle$, to be less than $< 10^{-8}$. The difference in release of both the total energy and angular momentum (in $+z$ direction) due to gravitational radiation is less than $< 4 \times 10^{-5}$. This comparison shows that the version difference does not have any impact for our study.

3.2 Dynamics

In this section, we show the effect of initial spin on the dynamics by looking at the time spent on the inspiral part of binary neutron star mergers and explain what mechanisms are responsible for the differences. The inspiral times are presented in Table 1. The properties of the remnants are presented in section 3.7.

3.2.1 Models $M_{tot} = 2.55M_{\odot}$

For $M_{tot} = 2.55M_{\odot}$, the $\chi = 0[1]$ and $\chi = 0.2$ cases are compared only at $t_{dyn,1}$, but other cases are also compared at $t_{dyn,2}$. All remnants are a supramassive neutron star.

The spin-orbit interaction is well known to be attractive (repulsive) for spins which are anti-aligned (aligned) with the orbital angular momentum. Campanelli et al. (2006); Etienne et al. (2009); Bernuzzi et al. (2014); Dietrich et al. (2017b). The attractive and repulsive behaviours were first shown in binary black hole mergers. The repulsive behaviour is called "orbital hang-up" Campanelli et al. (2006). We see that the spin-orbit interaction changes behaviour at a point between $\chi_{1,2} = 0.4$ and 0.65 and this new behaviour becomes stronger when going to higher spins. It should be noted that the observed changes in the behaviour of spin-orbit interaction most likely do not have a physical origin as two other works of compact binary mergers Campanelli et al. (2006); Etienne et al. (2009) do not show such reversal. The effect is most likely due to the initial data.

i) Even for models where the effective spin of the binary χ is the same, the individual spin magnitudes $\chi_{1,2}$ and their orientations are important. Comparison of the two models with zero effective spins, $\chi = 0[2]$ and $0[3]$, with the irrotational case shows that adding spin to the NSs decreases the inspiral time by ~ 5.13 ms for $\chi = 0[2]$. Increasing the spin from the $\chi_{1,2} = \pm 0.4$ to ± 0.65 decreases the inspiral time by ~ 2.76 ms compared to the irrotational case. This behavior indicates that there is a point between $\chi_{1,2} = 0.4$ and 0.65 , where the spin-orbit interaction changes behaviour.

ii) For anti-aligned cases, increasing the effective spin from $\chi = -0.2$ to -0.4 decreases the inspiral time by ~ 1.32 ms. Increasing the effective spin further from $\chi = -0.4$ to -0.65 increases the inspiral time by ~ 0.74 ms as compared to the $\chi = -0.2$ case. This supports the description of the change in the spin-orbit interaction for the anti-aligned spinning cases.

iii) For models with aligned spins, increasing the effective spin from $\chi = 0.2$ to 0.4 increases the inspiral time by ~ 0.47 ms. Increasing it further from $\chi = 0.4$ to 0.67 decreases the inspiral time by ~ 2.55 ms as compared to the $\chi = 0.2$ case. This shows that the same behaviour is also seen for cases where the spins are aligned.

3.2.2 Models $M_{tot} = 3.05M_{\odot}$

For $M_{tot} = 3.05M_{\odot}$ the irrotational cases are only compared at $t_{dyn,1}$, due to prompt collapse to a BH, but the spinning cases are also compared at $t_{dyn,2}$, as they experience a HMNS phase. The equal mass spinning model results in BH formation but the unequal mass spinning model is still a HMNS at the end of $t_{dyn,2}$.

The time spent in the inspiral depends on the mass ratio and spin. The spinning cases inspiral for a longer time than the irrotational cases for the same mass ratio.

3.2.3 Models $M_{tot} = 4.10M_{\odot}$

For $M_{tot} = 4.10M_{\odot}$ all configurations are compared at $t_{dyn,1}$ which corresponds to ~ 3.44 ms after BH formation. Although masses of the binaries are so high that all of them experience prompt collapse to a BH, systems with anti-aligned (aligned) spins experience shorter (longer) inspiral than in the irrotational case.

3.3 Evolution of Thermodynamic Properties

In the previous section, we describe the effect of spin on the orbital dynamics; now we will show the impact of these differences on the maximum rest-mass density and temperature of the matter. The densities are given in units of the nuclear saturation density, $\rho_{sat} = 2.7 \times 10^{14} \text{ g cm}^{-3}$ Lattimer (2012).

For models with $M_{tot} = 2.55M_{\odot}$, at $t_{dyn,1}$ we present snapshots in the $x - y$ plane of the temperature of the remnant and the inner parts of the disc in Fig. 1, the evolution of the rest-mass density in Fig. 2, and the electron fraction in Fig. 3 of the outermost part of the disc.

The aligned (anti-aligned) spins increase (decrease) the inspiral time and lead to a less (more) violent merger which reaches lower (higher) temperatures as compared to the equal mass, irrotational models with the same total mass. The change in the maximum rest-mass density and temperature affects the neutrino emission. Because the $\chi = -0.65$ case reaches the maximum rest-mass density and temperature among 9 cases, it also has the largest neutrino energy and luminosities. The increase in neutrino energies will decrease the pressure support against the gravity.

The impact of the spin magnitude and orientation on the maximum rest-mass density does depend on the total mass, unlike for the values of the maximum temperature.

The remnant of the anti-aligned (aligned) spinning cases have clearly higher (lower) core temperature than for the irrotational case. Temperature at the centre of the core is ~ 15 MeV for the irrotational case, increases to ~ 65 MeV for $\chi = -0.65$ and decreases to ~ 7 MeV for $\chi = 0.67$.

Even though the maximum rest-mass density reached for aligned spins are lower than the irrotational case for $M_{tot} = 2.55M_{\odot}$, it is higher for $M_{tot} = 3.05$ and $4.10M_{\odot}$ cases. If the total mass of the binary is so high that it collapses to a BH, either promptly or the delayed, the maximum density values for the aligned models are greater than in the irrotational case. Aligned spins result in the formation of spiral arms whose strength increases with spin. Anti-aligned (aligned) spinning - irrotational cases result in tidal disruption of the neutron star for which the tidal tail is more apparent for the aligned spinning-irrotational case. The $\chi = 0[3]$ case shows the most prominent tidal tail.

As can be seen in Fig. 3 the presence of spin changes the thermodynamic properties of the system depending on its magnitude and orientation and the resulting electron fraction distributions differ

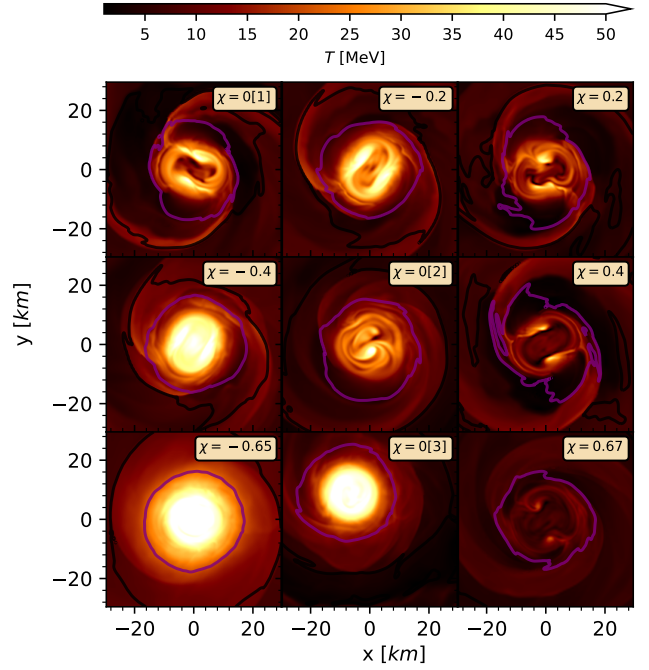


Figure 1. Snapshots of temperature distribution of the remnant and the innermost part of the disc for $M_{tot} = 2.55M_{\odot}$ at time $t_{dyn,1}$ in the $x - y$ plane. The effective spin for each panel is specified within the upper right of each plot. The purple contour shows the location of $\rho = 10^{13} \text{ g cm}^{-3}$. Black contours show the rest-mass density of 10^{11} and $10^{12} \text{ g cm}^{-3}$.

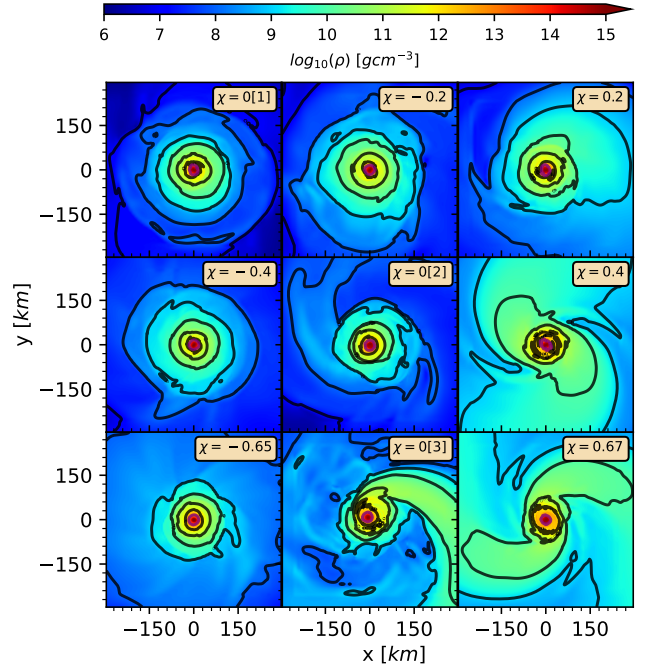


Figure 2. Snapshots of the rest-mass density distribution for $M_{tot} = 2.55M_{\odot}$ in the $x - y$ plane at time $t_{dyn,1}$. Black contours show the rest-mass densities $\rho = 10^6, 10^7, 10^8, 10^9, 10^{10}, 10^{11}, 10^{12} \text{ g cm}^{-3}$ and the purple contour shows $\rho = 10^{13} \text{ g cm}^{-3}$. Note the tidal tail for case $\chi = 0[3]$ and the tidal arms for case $\chi = 0.67$.

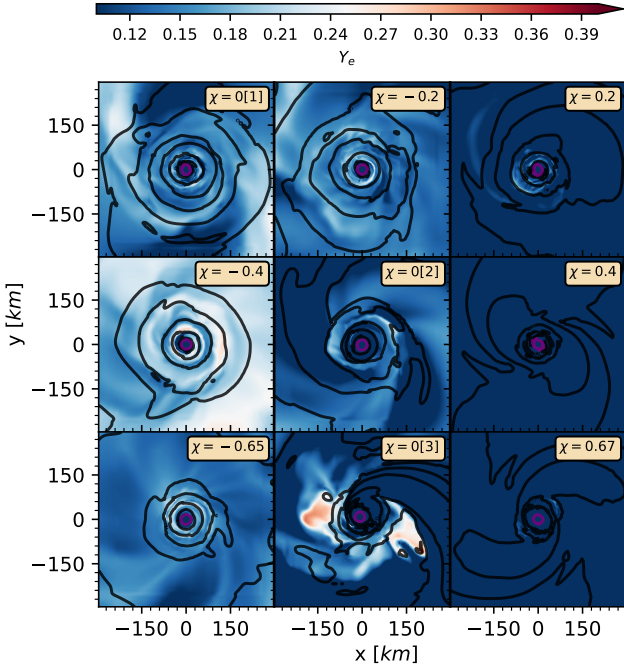


Figure 3. The electron fraction distribution is colour coded, while the contours are the same as in Fig. 2.

accordingly. Tidal tails and spiral arms are mainly composed of neutrons. Anti-aligned (aligned) spinning models are less (more) neutron rich than the irrotational models.

3.4 Neutrinos

Using the $M0$ scheme, details of which can be reviewed in Sect. 2, we will now show the effect of spin on the average neutrino energy and peak neutrino luminosity for the electron neutrino (ν_e), electron antineutrino ($\bar{\nu}_e$) and the heavy-lepton neutrinos (ν_μ). We present the average neutrino energy and peak neutrino luminosities for all flavours in Tables A1 and A2, respectively.

The neutrino emission shuts off for model $\chi = 0[3]$ at $\sim 1.5\times$ dynamical time before $t_{dyn,1}$. For all models $\langle E_\nu \rangle$ reaches a maximum for ν_μ and a minimum for $\bar{\nu}_e$, except for $M_{tot} = 4.10M_\odot$. The anti-aligned spinning cases have higher neutrino energies than the aligned spinning cases, if the remnant does not promptly collapse to a BH. With increasing spin the neutrino energies increase for equal and unequal mass binaries for models with $M_{tot} = 3.05M_\odot$. For models $M_{tot} = 2.55M_\odot$ the L_ν^{peak} is reached for ν_μ for the irrotational and anti-aligned spinning cases, except for $\chi = -0.65$ and $\bar{\nu}_e$ for the aligned spinning cases. The L_ν^{peak} decreases with spin, but increases with mass ratio.

Neutrinos change the composition of the matter through weak interaction and affect the stability of the remnant SMNS and HMNS by carrying energy away. The change in neutrino energies will affect the stability of the SMNS and HMNS, their mass, velocity, composition and distribution of the ejected matter, all of which will determine the gravitational waveform, the r-process nucleosynthesis and the ensuing kilonova (see Foucart (2023) for a recent review of the impact of neutrinos in binary neutron star mergers).

3.4.1 Models $M_{tot} = 2.55M_\odot$

For models with $M_{tot} = 2.55M_\odot$ the average neutrino energies are highest for the heavy-lepton neutrinos at $\sim 24 - 31\text{MeV}$ and lowest for the electron neutrinos at $\sim 12 - 17\text{MeV}$. The average neutrino energies are higher for anti-aligned spinning cases and lower for the aligned spinning cases as compared to the irrotational models. That applies for all flavours. For the $\chi = 0[3]$ case neutrino emission shuts off at $\sim 1.5\times$ dynamical time before $t_{dyn,1}$.

3.4.2 Models $M_{tot} = 3.05M_\odot$

For $M_{tot} = 3.05M_\odot$ the highest neutrino energies are between ~ 10 and 23MeV and correspond to the heavy-lepton neutrinos, similarly to binaries with $M_{tot} = 2.55M_\odot$.

By time $t_{dyn,1}$ the irrotational cases have collapsed to a BH while the spinning cases still are HMNS. As the only contribution to the neutrino energies are due to the disc for BH models, they have lower energies compared to the spinning models. Tidal disruption results in increase in neutrino energies for all flavours compared to the equal mass irrotational case. Increasing the mass ratio from $q = 1$ to $q = 2.05$ for spinning cases increases the total neutrino energy for all flavours.

By $t_{dyn,2}$ the equal mass spinning models collapse to a BH and the unequal mass spinning models are still a HMNS. A comparison of the equal mass irrotational case with the equal mass spinning cases after BH formation shows that the latter has higher energy neutrinos for all flavours than the former, due to the presence of a massive disc.

For the unequal mass spinning models the neutrino emission shuts off at $\sim 53\times$ dynamical time after $t_{dyn,1}$.

3.4.3 Models $M_{tot} = 4.10M_\odot$

For $M_{tot} = 4.10M_\odot$ at $t_{dyn,1}$, the highest neutrino energies are $\sim 0.7 - 7\text{MeV}$, where the upper bound relates to heavy-lepton neutrinos in the aligned spinning case. As all models experience prompt collapse to a BH, the disc mass and turbulence lead to differences in neutrino energies and changes of flavour. It is noteworthy that all cases except for the mixed spinning case have the highest neutrino energies for the heavy-lepton neutrinos and lowest energies for the electron neutrinos, similar to other models with $M_{tot} = 2.55$ and $3.05M_\odot$. However, the mixed spinning case has the lowest and the highest energies for heavy-lepton neutrinos and electron antineutrinos, respectively.

3.5 Gravitational waves

In this section we will show the impact of spin on gravitational waves by looking at energy and angular momentum loss (in +z direction), peak luminosity, frequency and spectra of the gravitational waves. We consider modes up to $(l, m) = (8, 8)$ and discuss their detectability at a distance of 100Mpc by the Advanced LIGO Collaboration et al. (2015) and the Einstein Telescope (ET) Maggiore et al. (2020).

In Tables A3 and A4 we present the total energy and angular momentum loss due to gravitational waves, the ratio of the energy and angular momentum release during the inspiral to the total energy and angular momentum release, and the ratio of the total energy and angular momentum release to the total initial mass (energy) and angular momentum, respectively.

The aligned spinning cases lead to higher energy loss than the irrotational case for $M_{tot} = 3.05$ and $4.10M_\odot$. The maximum energy is radiated by the irrotational case for $M_{tot} = 2.55M_\odot$. For this total

mass, aligned spinning cases have higher energy loss than the anti-aligned spinning cases with the same spin magnitude.

The frequencies of modes which contribute to total energy by more than 2×10^{-3} are presented in Table 2.

The gravitational wave strains from 9 equal-mass cases that resulted in a SMNS formation are shown in Fig. 4. The effect of spin on the dynamics is clearly reflected in the gravitational wave strains whose maximum correspond to retarded merger times $t - r = 0$. During the inspiral part, changes in dynamics are clearly reflected in the signal. During post-merger, the spin magnitude and orientation have a crucial effect on oscillations of the remnant, mimicking the behaviour of BNS mergers with softer or stiffer EOS. During merger, spin results in increase (decrease) of the strain amplitude by at most 10 and 21 per cent, for $\chi = 0.4$ and $\chi = -0.4$ cases, as compared to the irrotational case.

Gravitational waves are calculated by the `WeylSca14` and `Multipole` thorns of the `Einstein Toolkit`. While the former is used to compute the Newman-Penrose curvature scalar Ψ_4 , the latter is used to decompose the scalar into $s = -2$ spin-weighted spherical harmonic modes on a sphere with a radius of ~ 443 km. The strain is computed from the double time integration of Ψ_4 using the Fixed Frequency Integration (FFI) [Reisswig & Pollney \(2011\)](#)

$$h = h_+^{lm}(r, t) - ih_\times^{lm}(r, t) \\ = \int_{-\infty}^t du \int_{-\infty}^u dv \Psi_4^{lm}(r, v) \quad (2)$$

where h_+ and h_\times represent the plus "+" and cross "x" polarization of the gravitational waves. The quantity Ψ_4 is given as

$$\Psi_4(t, r, \theta, \phi) = \sum_{l=2}^{l=8} \sum_{m=-l}^l \Psi_4^{lm}(t, r) {}_{-2}Y_{lm}(\theta, \phi) \quad (3)$$

3.5.1 Energy and angular momentum release

The energy and angular momentum release due to gravitational radiation are presented in Table A3 and in Table A4, respectively.

The aligned spinning cases lead to higher angular momentum loss than the irrotational case for $M_{tot} = 3.05M_\odot$, except for the unequal mass cases, and $4.10M_\odot$. The maximum angular momentum is radiated by the irrotational case for $M_{tot} = 2.55M_\odot$. For this total mass, aligned spinning cases have higher angular momentum loss than the anti-aligned spinning cases.

For $M_{tot} = 2.55M_\odot$ irrotational models the highest total energy and angular momentum release are $6.85 \times 10^{52} \text{ ergs}$ and $1.37 M_\odot^2$. The aligned spinning cases release higher energy & angular momentum than the anti-aligned cases with the same spin magnitude. The case for $\chi = \pm 0.4$ mark a point where the energy & angular momentum release increases (decreases), if it was decreasing (increasing) from $\chi = -0.2$ to this spin magnitude.

The emergence of the (2, 1) mode during the inspiral is only seen for $\chi = \pm 0.2, 0[2], 0[3]$ cases. Among these cases, the remnant of the $\chi = 0[2]$ case shows the quasi-periodic oscillation, with a period and amplitude of ~ 0.7 ms and $\sim 6 \times 10^{-24}$, assuming a distance of 100 Mpc. The period corresponds to approximately twice the maximum frequency of the fundamental mode.

For models with $M_{tot} = 3.05M_\odot$ the total energy and angular momentum release substantially changes with mass ratio and spin, the highest energy and angular momentum release are $\sim 12 \times 10^{52} \text{ ergs}$ and $2.22M_\odot^2$. This corresponds to the equal mass spinning case. Spinning models have higher inspiral and post-merger energy and angular momentum release compared to the irrotational cases. The

energy and angular momentum release decreases as the mass ratio increases for both the irrotational and spinning cases. The decrease in energy is ~ 50 per cent for the irrotational cases and reaches up to ~ 80 per cent for the spinning cases.

The comparison of the gravitational wave strain between equal and unequal mass cases shows that the amplitude drastically decreases for the unequal mass cases.

For models with $M_{tot} = 4.10M_\odot$ the aligned spinning case has the highest energy and angular momentum release at $\sim 13 \times 10^{52} \text{ ergs}$ and $3.07 M_\odot^2$. Even though the anti-aligned spinning case has the shortest inspiral time, it emits ~ 15 per cent more energy and 0.2 per cent less angular momentum than the irrotational case during inspiral.

3.5.2 Frequency and spectra

We show the effect of spin on the instantaneous frequency at the instant merger f_{merger} and the post-merger peak frequency $f_{l,m}^{peak}$, for different modes. We present the merger and the peak frequencies in Table 2. In this table we only provide the instantaneous merger frequencies for the binaries that promptly collapse to the BH and $f_{2,0}^{peak}$ for $\chi = 0.67$ at the highest resolution because the difference between the two resolution is greater than 100 per cent. The gravitational wave spectra are highly sensitive to numerical resolution. As the peak frequency for the (2, 0) mode does not converge between the two resolutions, we assume the highest resolution to be closer to the actual value.

The merger and peak frequency for (2, 1) mode increases up to ~ 1.5 kHz, and ~ 1 kHz, for $\chi = -0.65$, compared to the irrotational case, respectively. The change in peak frequencies of the (2, 2) and (3, 3) modes are at most ~ 0.4 kHz for the $\chi = -0.65$ cases. The shift in the gravitational wave frequency of the (2, 0) mode increases by ~ 4 kHz for the $\chi = 0.2$ case as compared to the irrotational case.

For models with $M_{tot} = 2.55M_\odot$ the merger frequency increases as the spin increases for the anti-aligned spinning cases. We see that the peak frequency of the fundamental mode, $f_{2,2}^{peak}$, shifts to lower frequencies for both aligned models. This supports the findings of [Bernuzzi et al. \(2014\)](#); [Dietrich et al. \(2017a\)](#); [East et al. \(2019\)](#). The anti-aligned cases shift frequencies more than the aligned cases and the maximum shift by the irrotational case $\chi = -0.65$ reaches to 0.42 kHz. The shift to the lower frequencies for the anti-aligned case is unlike what was reported in [East et al. \(2019\)](#) where the spin of $\chi = -0.13$ is considered. The difference could be due to high spins of $\chi = -0.4$ and $\chi = -0.65$, we consider in our study.

The comparison of equal and unequal mass spinning cases with $M_{tot} = 3.05M_\odot$ shows that with increasing mass ratio the peak frequency for the fundamental mode shifts to higher frequencies by ~ 0.05 kHz.

For models with $M_{tot} = 3.05M_\odot$ the merger frequency increases by at most ~ 8 per cent for the spinning binaries as compared to the irrotational ones, and decreases by at most ~ 15 per cent for the unequal mass cases as compared to the equal mass cases.

For models with $M_{tot} = 4.10M_\odot$ the merger frequency is 2.37 kHz for the irrotational case and it increases by ~ 29 per cent for the $\chi = -0.65$ case and decreases by ~ 27 per cent for the $\chi = 0.67$ case, as compared to the irrotational case.

The gravitational wave spectra for modes (2, 1) and (2, 2) for models with $M_{tot} = 2.55M_\odot$ along with the sensitivity curves of the gravitational wave detectors Advanced LIGO and Einstein Telescope (ET) are presented in Fig. 6 and in Fig. 5, respectively. As can be seen in Fig. 6 increasing the spin for the anti-aligned case shifts the peak

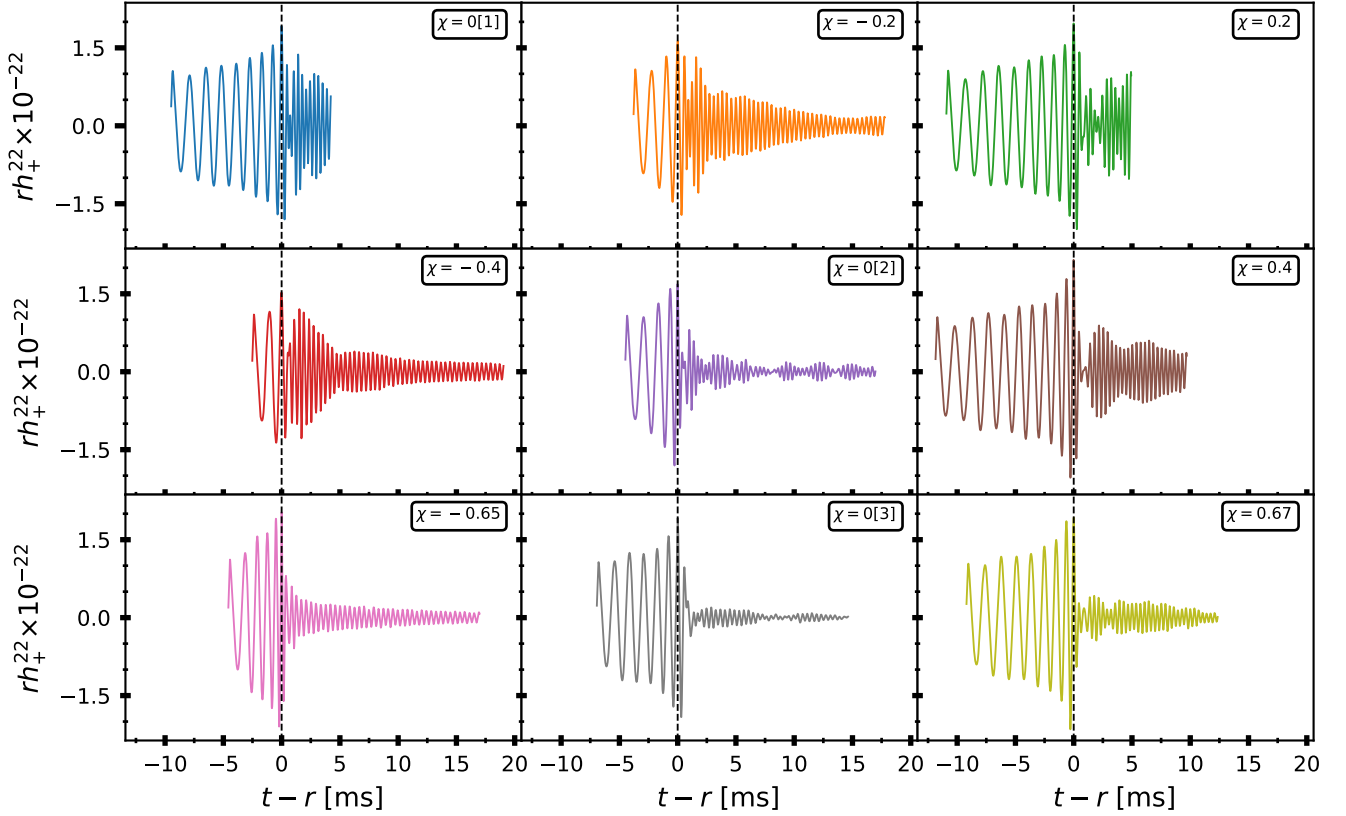


Figure 4. Effect of spin on the $(l, m) = (2, 2)$ mode of h_+ polarization of the gravitational wave strain (multiplied by the extraction radius of 443km) at a distance of 100Mpc. The vertical black dashed lines show the retarded merger times, $t - r = 0$, which are identified as the maximum of the strain.

Table 2. Gravitational wave frequencies for modes whose contribution to the total gravitational wave energy is greater than 2×10^{-3} . The merger frequencies f_{merger} correspond to the instantaneous frequency at the time of merger and $f_{l,m}^{\text{peak}}$ present the peak gravitational wave frequencies for the specified (l, m) mode. For remnants that promptly collapse to a BH we only state the merger frequencies. The values given with \pm show the difference between the models with two numerical resolutions. For $M_{\text{tot}} = 2.55M_{\odot}$ all frequencies are given with the difference between the two resolutions, except for $\chi = 0.67$ case for which only the highest resolution for the $(2, 0)$ mode is given.

Model	f_{merger}	$f_{2,0}^{\text{peak}}$	$f_{2,1}^{\text{peak}}$	$f_{2,2}^{\text{peak}}$	$f_{3,3}^{\text{peak}}$
$\chi = 0[1]$	1.41 ± 0.42	1.25 ± 0.95	1.43 ± 0.12	2.85 ± 0.00	3.86 ± 0.12
$\chi = -0.2$	1.25 ± 0.08	1.22 ± 0.04	1.42 ± 0.00	2.68 ± 0.08	4.06 ± 0.08
$\chi = 0.2$	2.35 ± 0.57	5.54 ± 1.58	1.37 ± 0.05	2.80 ± 0.05	4.12 ± 0.16
$\chi = -0.4$	1.30 ± 0.10	1.22 ± 0.85	1.43 ± 0.05	2.68 ± 0.12	4.02 ± 0.20
$\chi = 0[2]$	2.07 ± 0.22	5.42 ± 2.08	1.34 ± 0.08	2.69 ± 0.16	4.11 ± 0.16
$\chi = 0.4$	1.66 ± 0.50	4.46 ± 0.49	2.60 ± 1.22	2.80 ± 0.00	4.18 ± 0.16
$\chi = -0.65$	2.87 ± 0.07	1.70 ± 0.00	2.43 ± 1.74	2.43 ± 0.08	3.45 ± 0.40
$\chi = 0[3]$	1.56 ± 0.03	1.66 ± 0.00	2.56 ± 0.12	2.56 ± 0.12	2.56 ± 0.08
$\chi = 0.67$	2.05 ± 0.53	1.62^*	1.38 ± 0.01	2.80 ± 0.00	4.18 ± 0.00
305q1 χ 0	1.58	-	-	-	-
305q1 χ 0.4	1.66	2.82	1.68	3.26	4.59
305q205 χ 0	1.36	-	-	-	-
305q205 χ 0.4	1.47	1.74	1.63	3.31	3.23
41q1 χ 0[1]	2.37	-	-	-	-
41q1 χ 0[2]	2.45	-	-	-	-
41q1 $\chi - 0.65$	2.74	-	-	-	-
41q1 χ 0.67	1.73	-	-	-	-

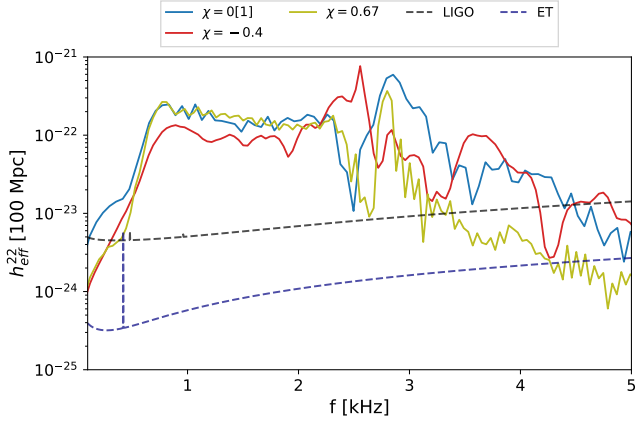


Figure 5. Gravitational wave spectra of the fundamental mode $(l, m) = (2, 2)$ for models with $M_{tot} = 2.55M_{\odot}$ and their detectability by the Advanced LIGO and the Einstein Telescope (ET); for sensitivity curves see [Evans et al. \(2020\)](#). The dotted lines show the sensitivity curves of the detectors.

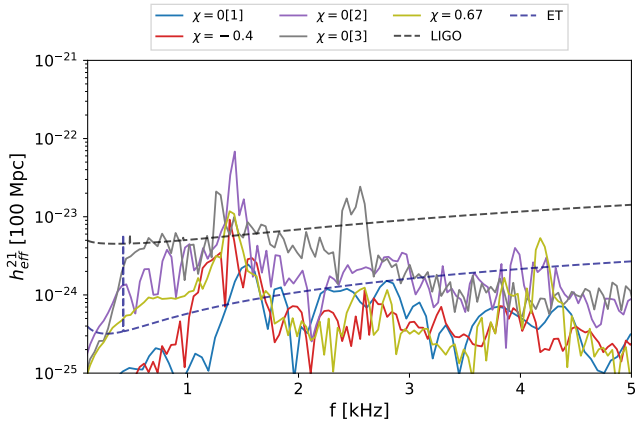


Figure 6. A similar presentation as in Fig.5 but for mode $(l, m) = (2, 1)$. It also includes the $\chi = 0[2]$ and $0[3]$ cases.

frequencies to lower frequencies as much as 0.42 kHz. The difference in peak frequencies is small for aligned spin cases as compared to the irrotational case. For higher frequencies beyond the peak the effective strain is suppressed for the $\chi = 0.67$ case. Fig. 5 shows that the maximum effective strain is reached at ~ 1.34 kHz which is a shift of ~ 0.12 kHz as compared to the irrotational case for $\chi = 0[2]$. The peak frequency shifts to higher frequencies by 1.23 kHz, as compared to the irrotational case for $\chi = 0[3]$.

3.6 Ejecta properties

We calculate the ejected matter properties, unbound matter that does not fall back, from a surface placed at ~ 443 km. We use the `OutFlow` thorn with the geodesic criteria [Kastaun & Galeazzi \(2015\)](#) $u_t < -1$, where u_t is the time component of the four-velocity. The ejected matter properties are presented in Table 3. Time calculations are performed in the frame of reference of the binary. Electron fraction and velocity of the matter are given as mass-weighted averages. The presence of fast-moving ejecta, which we identify to be ejecta moving with mass weighted velocity equal to or greater than 0.6c ([Radice et al. \(2018\)](#) and references therein) is presented for a number of cases. The total mass of the ejected matter increases for the all

considered spin magnitudes and orientations, except for many of the $M_{tot} = 4.10M_{\odot}$ models. It reaches $\sim 0.085M_{\odot}$ for the extreme aligned spin case $\chi = 0.67$.

3.6.1 Models with $M_{tot} = 2.55M_{\odot}$

For models with $M_{tot} = 2.55M_{\odot}$ all spin configurations result in higher total mass of the ejected matter as compared to the irrotational case and the mass increases as the spin increases. The total ejected mass at $t_{dyn,1}$ is $\sim 0.5 \times 10^{-3}M_{\odot}$ for the irrotational case. It reaches $\sim 0.06M_{\odot}$ and further increases to $\sim 0.085M_{\odot}$ at $t_{dyn,2}$, for the $\chi = 0.67$ case. For the anti-aligned and aligned spinning cases the ejected matter moves with higher and lower velocities as compared to the irrotational case, respectively, except for $\chi = -0.65$ case.

Even though fast-moving ejecta are not present in the irrotational and aligned spinning cases they are present for the anti-aligned spinning cases and their mass increases with spin. The fast-moving ejecta are also present in the mixed spin model $\chi = 0[3]$, but the difference between the two resolutions did not converge. The composition becomes more neutron-rich than the irrotational case for all cases.

3.6.2 Models with $M_{tot} = 3.05M_{\odot}$

For models with $M_{tot} = 3.05M_{\odot}$ we mention the effect of spin for the two times $t_{dyn,1}$ and $t_{dyn,2}$ separately. Note that, we compare equal and unequal mass spinning and irrotational cases separately. The equal mass spinning case is compared with unequal mass spinning case at $26\times$ dynamical time which is $= t_{dyn,1}$ for these cases. Once the equal mass spinning case collapses to a BH, we compare it with other BH cases at ~ 1.79 ms after BH formation. This is the $t_{dyn,2}$ for the equal mass spinning case. For the unequal mass spinning case $t_{dyn,2}$ corresponds to $95\times$ dynamical time.

At time $t_{dyn,1}$, an increase of the mass ratio decreases the total mass of the ejected matter for both the irrotational and the spinning cases.

The comparison between equal mass spinning and equal mass irrotational cases show that the mass of the ejected matter is higher for the former than the latter, and reaches $\sim 0.01M_{\odot}$, whereas for the latter it reaches $\sim 0.06 \times 10^{-3}M_{\odot}$. The mass weighted average electron fraction and velocity of the ejected matter is lower for the spinning case than for the irrotational case.

We only see the presence of the fast-moving ejecta for the unequal mass spinning case with a mass of $\sim 0.42 \times 10^{-5}M_{\odot}$. The fast moving-ejecta are very neutron-poor with the mass-weighted average electron fraction of $\langle Y_e \rangle = 0.41$.

3.6.3 Models with $M_{tot} = 4.10M_{\odot}$

For models with $M_{tot} = 4.10M_{\odot}$, the total ejected mass is highest at $\sim 3.95 \times 10^{-3}M_{\odot}$ for the spin-aligned case. In the irrotational case, unlike for the other equal mass irrotational cases with $M_{tot} = 2.55M_{\odot}$ and $3.05M_{\odot}$, the fast-moving ejecta is present and has a mass of $\sim 0.2 \times 10^{-3}M_{\odot}$. For the irrotational case, the composition of the fast-moving ejecta is very similar to the total ejecta with a mass-weighted average electron fraction of ~ 0.37 . On the other hand, the composition of the total ejecta is the most neutron-rich, with a mass-weighted average electron fraction of ~ 0.10 . It moves at the mass-weighted average velocity of $0.40c$ for the aligned spinning case.

Table 3. The properties of ejected matter for all models at two dynamical times $t_{dyn,1}$ and $t_{dyn,2}$ in the frame of reference of the binary, and disc masses at $t_{dyn,2}$ if extant (see section 3 for the definition of these times). The ejecta properties are extracted at a surface located at a distance $r = 443\text{km}$. M_{ej} and $M_{ej} \geq 0.6c$ show the total mass of the ejecta and the fast-moving ejecta (Radice et al. (2018) and references therein), M_{disc} , $\langle v \rangle$ and $\langle Y_e \rangle$ represent the disc mass, mass-weighted average velocity, and electron fraction of the ejecta, respectively. We provide disc masses only for a resolution of $h = 307\text{m}$ for binaries with $M_{tot} = 2.55M_\odot$. The values given with \pm show the difference between two resolutions.

Model	$M_{ej} (10^{-3}M_\odot)$		$M_{ej} \geq 0.6c (10^{-5}M_\odot)$		M_{disc} ($10^{-3}M_\odot$)	$\langle Y_e \rangle$		$\langle v \rangle (c)$	
	$t_{dyn,1}$	$t_{dyn,2}$	$t_{dyn,1}$	$t_{dyn,2}$		$t_{dyn,1}$	$t_{dyn,2}$	$t_{dyn,1}$	$t_{dyn,2}$
$\chi = 0[1]$	0.46 ± 0.09	-	0.00	-	127	0.27 ± 0.02	-	0.31 ± 0.03	-
$\chi = -0.2$	2.06 ± 0.24	3.40 ± 1.00	1.30 ± 1.20	1.30 ± 1.20	198	0.18 ± 0.00	0.18 ± 0.01	0.32 ± 0.01	0.26 ± 0.02
$\chi = 0.2$	1.20 ± 0.62	-	0.00	-	164	0.10 ± 0.05	-	0.23 ± 0.00	-
$\chi = -0.4$	3.32 ± 1.19	6.96 ± 2.62	1.42 ± 0.48	1.42 ± 0.48	130	0.26 ± 0.00	0.26 ± 0.01	0.35 ± 0.04	0.27 ± 0.02
$\chi = 0[2]$	0.75 ± 0.01	2.35 ± 0.97	0.00	0.00	134	0.17 ± 0.02	0.20 ± 0.04	0.25 ± 0.00	0.20 ± 0.01
$\chi = 0.4$	9.43 ± 0.33	24.29 ± 2.02	0.00	0.00	365	0.06 ± 0.00	0.06 ± 0.00	0.25 ± 0.00	0.20 ± 0.01
$\chi = -0.65$	12.03 ± 0.86	15.57 ± 0.48	26.00 ± 2.86	26.00 ± 2.86	251	0.21 ± 0.02	0.20 ± 0.01	0.31 ± 0.02	0.28 ± 0.01
$\chi = 0[3]$	48.82 ± 4.29	75.58 ± 3.73	0.01 ± 0.01	0.01 ± 0.01	221	0.05 ± 0.00	0.06 ± 0.00	0.26 ± 0.01	0.23 ± 0.00
$\chi = 0.67$	55.77 ± 8.83	85.37 ± 1.58	0.00	0.00	304	0.04 ± 0.01	0.05 ± 0.01	0.25 ± 0.01	0.22 ± 0.00
305q1 χ 0	0.064	-	0.00	-	0.839	0.31	-	0.31	-
305q1 χ 0.4	7.644	10.541	0.00	0.00	274	0.09	0.08	0.21	0.20
305q2.05 χ 0	0.009	-	0.00	-	179	0.29	-	0.26	-
305q2.05 χ 0.4	3.409	33.826	0.37	0.42	247	0.08	0.07	0.29	0.20
41q1 χ 0[1]	1.500	-	18.07	-	1.00	0.36	-	0.46	-
41q1 χ - 0.65	0.003	-	0.02	-	0.006	0.27	-	0.35	-
41q1 χ 0[2]	0.369	-	3.61	-	145	0.15	-	0.46	-
41q1 χ 0.67	3.948	-	0.00	-	363	0.10	-	0.40	-

3.7 Remnant properties

In this section we specify the impact of the initial spin on the structure of the remnant and investigate the supramassive (SMNS), hypermassive neutron star (HMNS) and black hole (BH) cases separately. The (quasi-local) mass and spin measurement are performed using `QuasiLocalMeasures` thorn, see Dreyer et al. (2003).

3.7.1 SMNS and HMNS

A differentially rotating neutron star was shown to support significantly more mass than an irrotational and uniformly rotating neutron star Baumgarte et al. (2000). All the remnants in models with $M_{tot} = 2.55M_\odot$ are SMNS and the unequal mass, spinning case with $M_{tot} = 3.05M_\odot$ is a HMNS. Both have a slowly rotating core with a rapidly rotating envelope, see Fig. 7. The rotation pattern of the BNS remnant is different from a single neutron star with constant j , see Shibata et al. (2005); Kastaun & Galeazzi (2015).

For models with $M_{tot} = 2.55M_\odot$ the irrotational, $\chi = \pm 0.2, \pm 0.4$ and 0.67 cases show a bar-like structure, where the envelope is hotter than the core. The other three cases, $\chi = 0[2], 0[3]$ and -0.65 , display spherical structure. The two cores quickly merge into one, for binaries with anti-aligned spins, as well as for binaries undergoing tidal disruption.

The remnants of the anti-aligned (aligned) spinning models have higher (lower) core temperature as compared to the irrotational case (see Fig. 1). The maximum temperature at the centre of the core of the remnant is $\sim 15\text{MeV}$ for the irrotational model and reaches $\sim 67\text{MeV}$ for the $\chi = -0.65$ case. It is only $\sim 7\text{MeV}$ for the $\chi = 0.67$ case. These differences clearly show the dependence of the thermodynamic remnant properties on the initial spin.

In every anti-aligned spinning case, neutron stars become highly elongated just before the two stars come into contact. Although the $\chi = 0.2$ case has ~ 30 per cent less total ejecta mass than the $\chi = -0.2$ case, it produces a more pronounced tidal tail (see Fig. 2).

For the $\chi = 0.2$ model we see mass transfer from the spinning

neutron star to the irrotational companion, which results in tidal disruption of spinning star. For the mixed spinning cases $\chi = 0[2]$ and $0[3]$, the neutron star that is tidally disrupted has spin aligned and anti-aligned with the orbital angular momentum, respectively. We also observe mass transfer for the $\chi = 0.4$ and 0.67 cases, both of which produce a spiral arm disc structure. It should be noted that the observed mass transfer could be due to the low resolution, as was reported in Dietrich et al. (2017b).

For the models with $M_{tot} = 3.05M_\odot$ spinning cases are at the HMNS state at time $t_{dyn,1}$. While the equal mass model collapses to a BH, the unequal mass case is still in the HMNS state at $t_{dyn,2}$. The equal and unequal mass cases reach maximum temperatures of $\sim 107\text{MeV}$ and $\sim 65\text{MeV}$ and rest-mass densities of $\sim 16\rho_{nuc}$ and $\sim 4\rho_{nuc}$, respectively.

3.7.2 The $m = 1$ instability

In this section, we discuss the $m = 1$ instability and show whether spin results in differences of the gravitational wave spectra.

In BNS mergers the $m = 1$ instability was first shown dynamically for an equal mass model with aligned spins with $\chi_{1,2} = 0.05$, see Paschalidis et al. (2015). A later study which considers eccentric BNS mergers reported the dependence of the $m = 1$ instability on spin. It showed that spins $\chi_{1,2} = 0.2$ are more favourable than higher spins, see East et al. (2016). These studies use a piecewise soft polytropic HB EOS from Read et al. (2009). The $m = 1$ instability was reported to be generic enough to arise even in quasi-circular irrotational BNS mergers using piecewise polytropic SLy and MS1b EOSs, see Radice et al. (2016a). The latter study reported that using mirror-symmetry for equal mass BNS mergers suppresses this instability.

Motivated by the findings of Radice et al. (2016a), we do not use mirror-symmetry for equal mass cases to reveal the conditions in which the $m = 1$ instability occurs.

We present the impact of the $m = 1$ instability on the gravitational spectra in Fig. 6. This instability is suppressed in particular for the $\chi = 0.4$ and $\chi = -0.65$ cases, both of which are not shown in

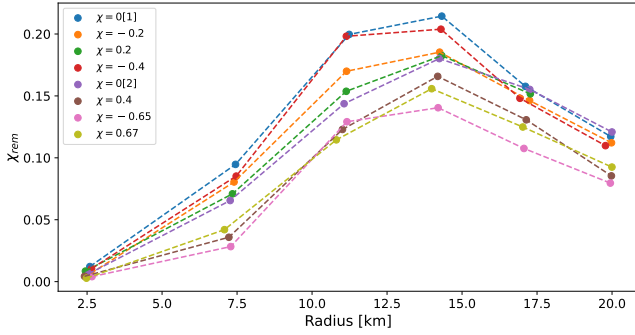


Figure 7. The quasi-local dimensionless spin of the post-merger remnant, following Tacik et al. (2015), where individual spins are monitored during the inspiral for models with $M_{tot} = 2.55M_{\odot}$ and for different initial spins. The circles show the maximum dimensionless spin reached for each case specified.

the plot. The $m = 1$ mode reaches its maximum effective strain for $\chi = 0[2]$ at ~ 1.42 kHz. The impact of initial spin on the peak frequency of the $m = 1$ mode is very low, except for models with $\chi = -0.65$ and $\chi = 0[3]$. While the former is suppressed, the latter could be important, in particular for the next generation detectors. The Einstein Telescope will be able to detect the $m = 1$ instability between 1 – 2 kHz for the $\chi = 0[1]$, -0.4 , $0[2]$, $0[3]$ and 0.67 cases.

3.7.3 Spin

In this section, we will show how the initial spin of the inspiralling binary stars affects the spin of the resulting SMNS and HMNS. In BNS mergers it was reported that even though the magnitude of the spin remains the same, its orientation changes during inspiral until the actual merger, see Tacik et al. (2015); Dietrich et al. (2017a).

The first application to BNS mergers of quasi-local angular momentum measurement was presented by Tacik et al. (2015). Following this application, we measure the quasi-local angular momentum from 6 ‘detectors’, 5 of which are placed at distances of ~ 1.48 km to ~ 16 km from the coordinate origin, where the latter distance approximately corresponds to the radius of SMNS and HMNS remnants for all models. The sixth radius is placed at a radius of ~ 29.5 km. The change of dimensionless spin parameter of the SMNS across the different radii is presented in Fig. 7. For the models with $M_{tot} = 2.55M_{\odot}$ until time $t_{dyn,1}$ the maximum and the minimum spin reaches 0.21 and 0.14, respectively, as extracted at a radius of ~ 14 km, for the irrotational and the $\chi = -0.65$ cases. We do not provide the spin measurement for $\chi = 0[3]$ because as we place radii to the coordinate origin, the remnant SMNS shifts from the origin which can be seen in Fig. 1.

For models with $M_{tot} = 3.05M_{\odot}$ the remnant of the equal and unequal mass spinning cases reach maximum spins of $\chi_{rem} \sim 0.40$ and $\chi_{rem} \sim 0.22$, respectively. The equal mass spinning case reaches $\chi_{rem} \sim 0.40$. This shows the spin of the remnant HMNS because the angular momentum in the outer parts of the remnant falls off. Effective transfer of angular momentum to the inner-parts eventually results in BH formation. The maximum spin of the unequal mass spinning model shows that the remnant spin values are not restricted to the equal mass binaries, but they are generic.

Table 4. The quasi-local mass and spin of the BH remnant at formation time t_{form} and at final times t_f . The time difference $t_{BH} - t_{merger}$ shows the BH formation time, where negative or positive sign indicate that the BH formed before or after the merger, respectively.

Model	$M_{BH} (M_{\odot})$		χ_{BH}		$t_{BH} - t_{merger} (ms)$
	t_{form}	t_f	t_{form}	t_f	
305q1 χ 0	2.92	2.98	0.79	0.83	+0.89
305q1 χ 0.4	2.15	2.63	0.43	0.71	+7.93
305q205 χ 0	2.34	2.73	0.27	0.55	+0.11
41q1 χ 0[1]	3.95	3.99	0.72	0.83	+0.17
41q1 χ 0[2]	3.13	3.78	0.39	0.79	+0.09
41q1 $\chi - 0.65$	3.96	3.80	0.50	0.69	-0.02
41q1 χ 0.67	3.05	3.57	0.79	0.92	+0.68

3.7.4 BH

We have 7 configurations that form BHs, 6 of which experience prompt collapse and the other one experiences a delayed collapse. The apparent horizons of the black holes are detected with AHFinderDirect, see Thornburg (1996, 2004); Brown et al. (2009). The quasi-local mass and the dimensionless spin parameter of the BH at time $t_{dyn,1}$ for all binaries experience prompt collapse and at time $t_{dyn,2}$ for the case that experiences delay collapse to the BH, are presented in Table 4. We also list the time difference between the BH formation and the merger, $t_{BH} - t_{merger}$. The delay in BH formation for prompt collapse models due to spin is also reported in a recent study by Schianchi et al. (2024). The BH remnant formed from binary neutron star mergers of the aligned spinning case with mass $M_{tot} = 4.10M_{\odot}$ is the fastest spinning BH with $\chi_{BH} = 0.92$, whereas for the irrotational case the BH spin value is ~ 0.83 .

The comparison of equal mass irrotational and spinning models to model $M_{tot} = 3.05M_{\odot}$, at time $t_{dyn,1}$ which corresponds to time $t_{dyn,2}$ for the spinning case, shows that for the spinning case the BH remnant has lower spin with $\chi_{BH} = 0.71$.

Due to the delayed collapse to a BH, the spin of the BH remnant decreases. This supports the restriction of the spin reported for the binaries experience HMNS phase to be $\chi_{BH} < 0.7 - 0.8$ Bernuzzi et al. (2016).

In the irrotational models, increasing the mass ratio substantially decreases the spin of the BH remnant, from $\chi_{BH} = 0.83$ down to 0.55. This is due to tidal disruption that leads to massive disc formation. The decrease in the spin of the remnant with increasing the mass ratio is in line with previous findings of Dietrich et al. (2017b).

For models with $M_{tot} = 4.10M_{\odot}$ the BH spin for the irrotational case is $\chi = 0.83$ at time $t_{dyn,1}$. The upper limit of the BH spin resulting from BNS mergers was reported to be, for an equal mass aligned spinning case, $\chi_{BH} = 0.888 \pm 0.018$ Kastaun et al. (2013). This upper limit for the spin of the remnant BH in the aligned spinning case reaches a value of 0.92 and becomes the fastest spinning BH resulting from BNS mergers, to date.

3.8 Disc structure

In this section, we discuss the distribution, composition and velocity of the matter in the disc, at time $t_{dyn,1}$, for the different total mass cases separately. We also present the impact of initial spin on disc masses.

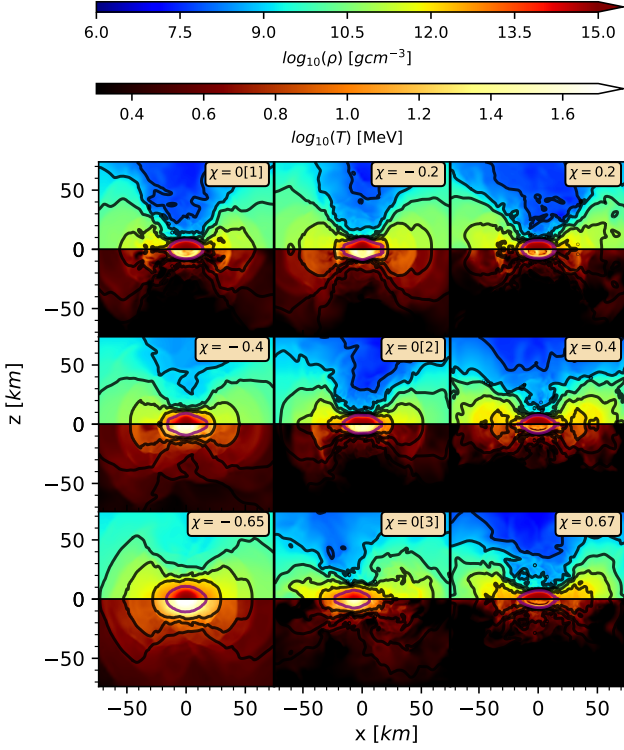


Figure 8. Snapshots of the rest-mass density and temperature showing the disc structure for models with mass $M_{tot} = 2.55M_{\odot}$ at time $t_{dyn,1}$ in the x - z plane. Contours show the rest-mass densities $\rho = 10^8, 10^9, 10^{10}, 10^{11}, 10^{12} gcm^{-3}$. The purple contour shows $\rho = 10^{13} gcm^{-3}$. Note that the temperature scale is different from Fig. 1. See text for further details comparing disc structure.

3.8.1 Models with $M_{tot} = 2.55M_{\odot}$

In Figs. 2 and 3 we present snapshots of the rest-mass density and the electron fraction at time $t_{dyn,1}$ and within ~ 300 km in x - y plane. We present the rest-mass density and temperature in Fig.8 and rest-mass density and electron fraction in Fig.9, both for the inner parts of the disc within ~ 75 km in the x - z plane.

In Fig.8 we see that the disc becomes more shock-heated as the temperature of the remnant increases. In Fig.9 we see that the aligned spinning cases are more neutron rich than the irrotational and anti-aligned spinning cases in the equatorial plane and in polar regions. Hence the aligned spinning cases lead to heavier r-process nucleosynthesis which yields dimmer kilonova than the irrotational and anti-aligned spinning cases, see Kasen et al. (2013).

For the irrotational case, the disc extends to a radius of ~ 180 km in the x - y plane. In this region the rest-mass density and the electron fraction are $\rho \sim 10^8 gcm^{-3}$ and $Y_e = 0.12 - 0.20$, respectively. All other cases have nearly similar disc extension, but differing composition, temperature and structure. The rest-mass density at the outermost part of the disc agrees with the irrotational case for all cases except for the aligned spinning cases $\chi = 0.4$ and 0.67 . The rest-mass density increases with the spin for these two cases and reaches $\rho \sim 10^{9.45}$ for $\chi = 0.67$ in the outermost part of the disc.

The presence of spin results in a tidal tail for models $\chi = 0.2, 0[2], 0[3]$ and in the formation of a spiral arm for $\chi = 0.4$ and 0.67 .

The comparison of the two aligned spinning cases $\chi = 0.4$ and 0.67 , shows the presence of two spiral arms, see Fig.2. The extent of the arm increases with amount of spin. The inner parts of the arms

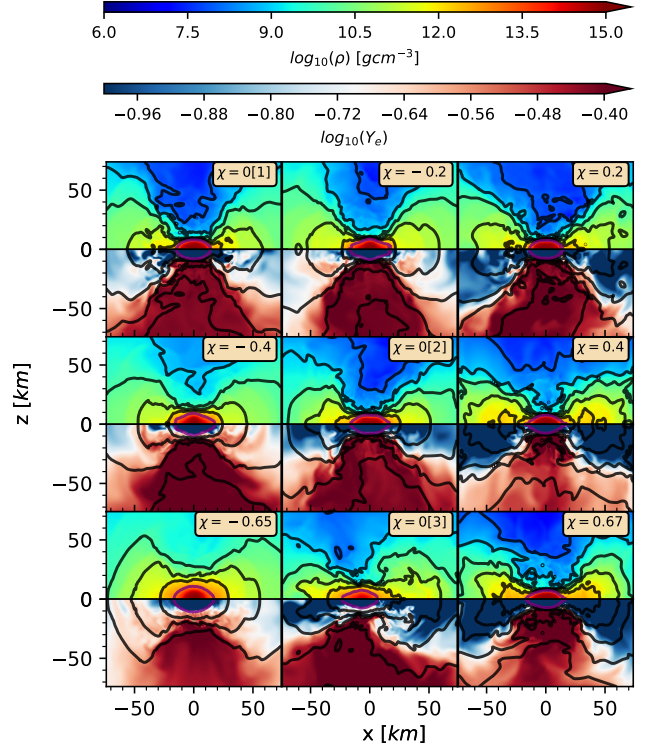


Figure 9. Snapshots of the rest-mass density and electron fraction of the inner parts of the disc and the remnant in the x - z plane. Contours are the same as in Fig.8. See text for further details comparing disc structure.

cover the remnant and mass is transferred from the arms to the region with rest mass density $\rho = 10^{11} gcm^{-3}$ (see Fig.8). The velocity of the matter reaches $\sim 0.20c$ at the place where the feeding stream hits the region with density $\rho = 10^{11} gcm^{-3}$. The composition of the spiral arms is very neutron rich with $Y_e \leq 0.05$, see Figs. 3 and 9. In the inner parts of the disc the electron fraction increases to 0.07 and 0.12 , at most, for the two cases $\chi = 0.4$ and 0.67 , respectively.

At time $t_{dyn,1}$ the model $\chi = 0[3]$ shows the most prominent one-sided tidal tail, see Fig.2. The tidal tail spirals around the remnant and transfers and increases the mass of the region where the rest-mass density reaches $\rho = 10^{12} gcm^{-3}$. The electron fraction of matter within the tidal tail increases to ~ 0.19 and moves with a velocity of $\sim 0.20c$. Among the 9 cases, model $\chi = 0[3]$ has the most neutron-poor component, reaching $Y_e = 0.33$ at a distance of 178 km from the origin on $-x$ axis. The temperature in the outermost part of the disc, including the tidal tail and spiral arm, is relatively cold with a temperature of $T < 2$ MeV for all cases.

Innermost part of the disc where the rest-mass density is $10^{12} \leq \rho \leq 10^{13} gcm^{-3}$, extends to a most ~ 14 km from the surface of the remnant for the irrotational case and extends to a maximum of ~ 27 km for model $\chi = 0.67$. This region is not very compact for models $\chi = -0.65, 0.4$ and 0.67 . The composition becomes only neutron-poor for $\chi = -0.65$ with at most $Y_e = 0.18$. This region is very neutron-rich with $Y_e = 0.05$ for models $\chi = 0.4$ and 0.67 . The velocity of the matter close to the surface of the remnant reaches the maximum value of $\sim 0.40c$ for all cases except for model $\chi = -0.65$ where the maximum velocity reaches $\sim 0.32c$.

For the irrotational case the remnant is covered by a layer of thickness 0.24 km where the rest mass density is $10^{12} \leq \rho \leq 10^{13} gcm^{-3}$. The thickness of this layer increases with spin for anti-

aligned spinning cases and reaches ~ 5 km for the $\chi = -0.65$ case. For the irrotational case the temperature reaches a maximum value of ~ 12 MeV for only a small part inside this region and other places are cold with a temperature of ~ 3 MeV.

The thickness of the inner part of the disc for which $10^{11} \leq \rho \leq 10^{12} \text{ g cm}^{-3}$, is ~ 19 km for the irrotational case and reaches at most ~ 31 km for the $\chi = -0.65$ case. The thickness is $\sim 18 - 25$ km for all other cases. The innermost disc structure is more turbulent for aligned spinning cases. They show an elliptical structure, as opposed to the anti-aligned spinning cases.

The temperature of this region increases (decreases) as the spin increases for anti-aligned (aligned) cases, respectively. It reaches ~ 28 MeV and ~ 11 MeV for models $\chi = -0.65$ and 0.67 , respectively.

3.8.2 Models with $M_{tot} = 3.05M_{\odot}$

For models with $M_{tot} = 3.05M_{\odot}$, in the equal mass irrotational case, the remnant BH is surrounded by an elongated disc which extends to a radius of $(r_x, r_y) = (70, 90)$ km. At the outermost part of the disc, the matter moves with $\sim 0.17c$, having the rest-mass density and the composition of $\rho \sim 10^8 \text{ g cm}^{-3}$ and between $Y_e = 0.20 - 0.29$, respectively.

The innermost part of the disc has a rest-mass density of $10^{10} \leq \rho \leq 10^{11} \text{ g cm}^{-3}$, a thickness of ~ 4 km and a temperature of $\sim 4 - 6$ MeV.

In this region the composition of the matter changes to $Y_e = 0.18 - 0.28$. The velocity of the matter at the outer part of this region exceeds $0.45c$ and very close to the remnant it increases to $0.73c$.

For the equal mass spinning model, two spiral arms are present and are being fed by the inner parts of the disc. The remnant is surrounded by matter with a rest-mass density of $\rho > 10^{12} \text{ g cm}^{-3}$.

For the unequal mass irrotational case, the remnant BH is fed by the tidal tail. The tail spirals around the remnant and increases the mass of the region with rest-mass density of $10^{12.40} \leq \rho \leq 10^{13.40} \text{ g cm}^{-3}$. The velocity of the matter along the tidal tail increases from ~ 0.22 to $\sim 0.45c$ close to the remnant. The composition of the tail and the region that directly surrounds the remnant is very neutron-rich with $Y_e \leq 0.05$ and is relatively cold with a temperature of ≤ 1 MeV, except for a very small region which is heated to ~ 4 MeV. At a distance of ~ 42 km from the origin we see the most neutron-poor part of the disc with $Y_e \sim 0.45$. Its rest-mass density is $\rho = 10^{8.26} \text{ g cm}^{-3}$ and it moves at $\sim 0.29c$. The matter in this region is relatively cold, with a temperature of $T = 1.5 - 3.0$ MeV. The velocity of the matter very close to the remnant increases to $\geq 0.62c$.

3.8.3 Models with $M_{tot} = 4.10M_{\odot}$

For models with $M_{tot} = 4.10M_{\odot}$ the only important disc formation is seen for the $\chi = 0.67$ case. As we have seen in the remnant properties section, such extreme spin configurations could even delay the prompt BH formation and produce a massive disc which has spiral arms feeding the remnant. The extent of the spiral arm is ~ 106 km in x - y plane. The spiral arm will eventually be absorbed into the BH or be ejected on a longer time-scale. The rest-mass density is $10^{11} \leq \rho \leq 10^{12} \text{ g cm}^{-3}$ throughout the arms and directly feed the innermost part of the disc. The composition of matter in the arm towards the innermost part of the disc $10^{11} \leq \rho \leq 10^{12}$ that surrounds the remnant is very neutron-rich with $Y_e \leq 0.05$ and the matter is relatively cold at $T < 1$ MeV. The velocity of the matter increases from $\sim 0.16c$ to ~ 0.52 close to the remnant. In a small region where the stream from the arm hits matter with rest-

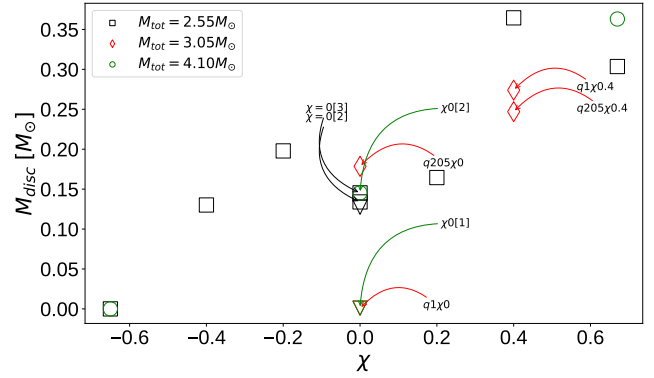


Figure 10. Effect of initial effective spin, χ , on the disk mass at $t_{dyn,2}$, if the disc mass exists at that time. Binaries with the total mass of $M_{tot} = 2.55M_{\odot}$, $3.05M_{\odot}$, and $4.10M_{\odot}$ are represented by black squares, red diamonds and green circles, respectively. The equal mass, irrotational cases are shown by triangles with colour corresponding to the total mass. The disc masses plotted for $M_{tot} = 2.55M_{\odot}$ have a resolution of $h = 307$ m. The most massive disc is formed for the case $\chi = 0.4$ with a mass of $\sim 0.36M_{\odot}$.

mass density $\rho = 10^{13} \text{ g cm}^{-3}$ the composition of the matter is $Y_e = 0.17 - 0.35$. There the temperature of the matter is $T = 8 - 10$ MeV.

The region with rest-mass density $10^{12} \leq \rho \leq 10^{13} \text{ g cm}^{-3}$ directly surrounds the remnant and has temperatures $T = 5 - 17$ MeV. The velocity of the matter is greater than $\sim 0.49c$ in this region.

3.8.4 Impact of spin on disc mass

In this section, we discuss the effect of initial effective spin on the disc mass. In order to calculate the baryonic mass of the disc, we integrate the mass with a rest-mass density below $\rho < 10^{13} \text{ g cm}^{-3}$, similarly to Radice et al. (2018) and references therein, see also Camilletti et al. (2024), within a radius of ~ 443 km. We calculate ejected matter properties therein. If a BH is formed, we remove the region with lapse function values lower than 0.3. The disc masses are given in Table 3, and the dependence of disc mass on the initial effective spin is shown in Fig. 10. In this figure, we provide the values of disc mass at time $t_{dyn,2}$, if the mass exists at that point in time. In Fig. 11 we show linear fits of the correlation between the sum of the individual spin magnitudes and disc mass, at time $t_{dyn,1}$. Although a correlation is clearly present, the fits display a big deviation due to low resolution. The fits are produced using linear regression through the least squares method.

For models with $M_{tot} = 2.55M_{\odot}$, we provide the disc masses at $t_{dyn,1}$ for $\chi = 0[1]$ and $\chi = 0.2$, and at $t_{dyn,2}$ for other models. For the latter models, disc masses decrease between times $t_{dyn,1}$ to $t_{dyn,2}$ for $\chi = -0.65$, $\chi = 0[3]$, and $\chi = 0.67$ cases, but increase for all other models. At $t_{dyn,1}$, all models except for $\chi = -0.4$ produce higher disc mass as compared to the irrotational model. In addition to that, aligned spinning models result in higher disc mass as compared to the anti-aligned spinning models with the same spin magnitude. However, both anti-aligned (aligned) spinning models produce a more (less) massive disc as the spin magnitude increases. We also see that, even though the effective spin is zero for three cases, $\chi = 0[1]$, $0[2]$ and $0[3]$, individual spins are important and the disc mass increases as the individual spin magnitude increases. The most massive disc is formed for the $\chi = 0.4$ model and reaches $\sim 0.36M_{\odot}$. The dependence of initial spin on disc mass, assuming one component is spinning, has also been presented by Papenfort et al. (2022); Rosswog et al. (2023, 2024).

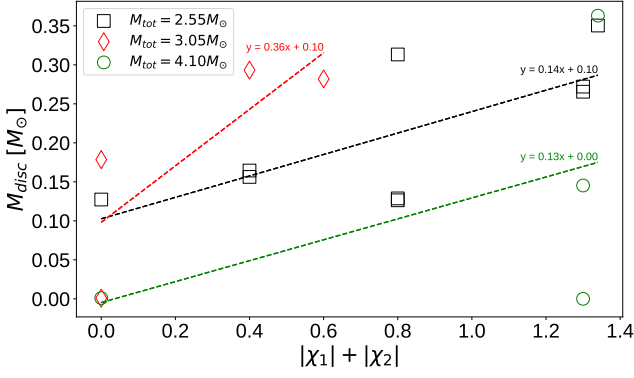


Figure 11. Linear fits of correlation between the sum of individual spin magnitude $|\chi_1| + |\chi_2|$ and disc mass, at $t_{dyn,1}$.

For models with $M_{tot} = 3.05M_{\odot}$, the comparison of equal and unequal mass irrotational models shows that even though they result in prompt black hole formation, the disc for the unequal mass model with $q = 2.05$ is much more massive. It has a mass of $\sim 0.18M_{\odot}$. Between times $t_{dyn,1}$ to $t_{dyn,2}$ disc masses decrease by $\sim 0.02M_{\odot}$ and $\sim 0.03M_{\odot}$, for equal and unequal mass spinning models, respectively. The most massive disc formed at $t_{dyn,2}$ is observed for the equal mass spinning model with a mass of $\sim 0.27M_{\odot}$. This is despite being simulated for a shorter time as compared to the unequal mass, spinning model.

For models with $M_{tot} = 4.10M_{\odot}$ the merger of the anti-aligned spinning model results in a disc with negligible mass, whereas both-aligned spinning model results in forming a much more massive disc as compared to the irrotational case. Its mass is $\sim 0.36M_{\odot}$.

4 SUMMARY AND CONCLUSION

We study the effect of the spin in BNS mergers. We consider 17 configurations with 3 different total masses and having both equal and unequal mass. Also spin configurations are varied, to cover cases where both stars' spins are aligned, or anti-aligned or mixed, with respect to the orbital spin. We investigate the impact of the initial spin on gravitational radiation emission, on properties of ejected matter and thermodynamic properties of all these systems as well as gravitational wave strains, their detectability, the maximum temperature and the rest-mass density of matter, the neutrino energy and their luminosities, and disc masses.

The presence of the spin has a crucial effect in orbital dynamics, its magnitude and orientation influences and changes the time spent during inspiral. In the work of [Kastaun et al. \(2013\)](#) they were the first to show the orbital hang-up effect for aligned spins in BNS mergers. The same phenomenon is later shown by [Tsatsin & Marronetti \(2013\)](#) and [Bernuzzi et al. \(2014\)](#), both of which studied equal mass stars. They used polytropic EOS in their simulations of BNS mergers and the spins of the stars where both anti-aligned or aligned with the orbital angular momentum. For aligned spin cases we see the same behaviour up to an effective spin of $\chi = 0.4$ due to spin-orbit interaction. Increasing the spin from $\chi = 0.4$ to $\chi = 0.67$ changes the behaviour of spin-orbit interaction, leading to a decrease in time spent in inspiral. For anti-aligned cases, while the inspiral time decreases up to $\chi = -0.4$, the time increases when increasing spin from $\chi = -0.4$ to -0.65 , showing the same behaviour observed as for the aligned cases.

Regarding the thermodynamic properties, anti-aligned (aligned) spinning cases experience more (less) violent mergers than the irrotational case, resulting in higher (lower) maximum temperature as compared to the irrotational case. For models with $M_{tot} = 2.55M_{\odot}$, the maximum temperature and the rest-mass density reached throughout the simulation is $T = 122\text{MeV}$ and $\rho = 5.75\rho_{sat}$, for case $\chi = -0.65$. We also noticed that when the spin magnitude increases the temperature increases (decreases) for anti-aligned (aligned) cases, respectively.

For models with $M_{tot} = 2.55M_{\odot}$ the average neutrino energies increase as the spin increases, for anti-aligned cases. For models with $M_{tot} = 3.05M_{\odot}$, the average neutrino energy increases with spin and mass ratio. The most energetic neutrino flavour is

- for $M_{tot} = 2.55M_{\odot}$ and $3.05M_{\odot}$: heavy-lepton neutrinos for all cases,
- for $M_{tot} = 4.10M_{\odot}$: electron anti-neutrinos for the irrotational case and the mixed spinning case $41q1\chi0[2]$, and heavy-lepton neutrinos for both aligned/anti-aligned spinning cases.

The energy and angular momentum release due to gravitational radiation depends on spin of the compact objects. The energy and angular momentum release for aligned spinning cases in models $M_{tot} = 3.05M_{\odot}$ and $4.10M_{\odot}$ is greater than the irrotational case within the same total mass, while the maximum energy and angular momentum release is obtained in the irrotational case for $M_{tot} = 2.55M_{\odot}$.

The peak frequencies for the fundamental mode are affected by spin and mass ratio. The post merger frequency of the fundamental mode shifts to lower frequencies for both anti-aligned and aligned spinning cases as compared to the irrotational case. The shifts in the anti-aligned spinning cases are greater than for the aligned spinning cases. The peak frequency shifts to the higher frequency for higher mass ratio.

The presence of spin changes the structure of the NSs during the merger. The formation of tidal tails or spiral arms is not seen in the equal mass irrotational BNS mergers. Four of our configurations for $M_{tot} = 2.55M_{\odot}$ have these features due to spin. We see the formation of spiral arms in models $\chi = 0.4$ and 0.67 and of tidal tails in models $\chi = 0.2$, $\chi = 0[2]$, and $0[3]$. The extent of the tidal tail for $\chi = 0.2$ is very small and the tail quickly dissolves. However, the spiral arms whose strength increases as the spin increases, extend to very large distances, for models $\chi = 0.4$ and 0.67 cases. The composition of the spiral arms and tidal tails are very neutron rich. This is a key parameter to determine the heavy r-process nucleosynthesis [Foucart \(2020\)](#). Our results of the effect of spin on the tidal disruption of a neutron star in equal mass binary neutron star mergers is in agreement with the studies of [Papenfort et al. \(2022\)](#); [Rosswog et al. \(2023, 2024\)](#) where only one component has a spin.

The total mass of ejected matter depends on the spin. The total mass ejected increases with increasing spin. Our study shows that high spins such as $\chi = 0.67$ could lead to having ejected masses of $\sim 0.085M_{\odot}$ even in the equal mass case. The presence of spin leads to fast-moving ejecta. Its mass increases as the spin increases in models $\chi = -0.2$ to -0.65 .

We have determined the final spin of the remnant, which is either a SMNS or a HMNS or a BH depending on the spin and mass ratio. A comparison shows that the SMNS remnant reaches the maximum dimensionless spin of ~ 0.21 for the irrotational case with mass $M_{tot} = 2.55M_{\odot}$. The HMNS remnant of an unequal mass merger with spinning stars and with $M_{tot} = 3.05M_{\odot}$ reaches $\chi_{rem} = 0.22$. This indicates that the maximum spin of the SMNS or the HMNS remnant does not change much with total mass or mass ratio, if does

not collapse to the BH. The core rotates slowly compared to the envelope Shibata et al. (2005); Kastaun & Galeazzi (2015).

The BH remnant of model 41 χ 0.67 reaches the dimensionless spin parameter of 0.92. This surpasses by ~ 1.5 per cent the previously presented upper limit from Kastaun et al. (2013), and becomes the highest dimensionless spin reached in BNS merger simulations. Even starting with a spin frequency very close to Keplerian frequency, the difference is only ~ 1.5 per cent.

We present the dependence of disc mass on the initial spin. Our simulations produce discs with mass $\sim 0.36M_{\odot}$ in cases of low (high) mass binary neutron star mergers, despite the latter promptly collapses to a BH. Even though both equal and unequal mass irrotational cases with $M_{tot} = 3.05M_{\odot}$ promptly collapse to a BH, the latter form a massive disc with mass $\sim 0.18M_{\odot}$. This elucidates the dependence of mass ratio on the disc mass. As the equal mass, spinning case with $M_{tot} = 3.05M_{\odot}$ experiences a hypermassive neutron star phase before finally collapsing to a BH, it has the most massive disc with mass $\sim 0.27M_{\odot}$. It is noteworthy to point out that mergers of equal high mass and rapidly spinning neutron stars yield a substantially massive disc with a mass of $\sim 0.36M_{\odot}$. This shows the importance of considering high spins on electromagnetic counterparts even for equal mass binaries that promptly collapse to a BH. Since disc mass is the quantity with the most impact on the kilonova peak luminosity, the correlation in Fig.11 suggests that one could use EM data to constrain $|\chi_1|+|\chi_2|$, breaking the degeneracy in the measurement of spin from gravitational wave alone.¹

The values of spin investigated in this study are higher than what is observed and we have shown the impact of such high spins on gravitational waves emission and properties of ejected matter. Hence, it is possible to distinguish them by gravitational wave observations. The differences in possible electromagnetic counterparts are not investigated here.

ACKNOWLEDGEMENTS

RM and BK would like to thank Ian Hawke for his comments/suggestions, guidance and support. BK would like to thank Roland Haas for his constant support, guidance and his useful comments/suggestions on every part of the study, David Radice for his many useful comments/suggestions, help and guidance, Wolfgang Tichy for his support and guidance, and Zachariah B. Etienne for his valuable comments.

The part of the study was presented at Thematic school GWsNS-2023: Gravitational Waves from Neutron Stars and at the European Einstein Toolkit Meeting 2023.

This work used TACC Stampede at XSEDE through allocation PHY160053 from the Extreme Science and Engineering Discovery Environment (XSEDE), which was supported by National Science Foundation grant number #1548562. The work has been performed under the Project HPC-EUROPA3 (INFRAIA-2016-1-730897), with the support of the EC Research Innovation Action under the H2020 Programme; in particular, BK gratefully acknowledges the support of The University of Edinburgh and the computer resources and technical support provided by EPCC. The numerical calculations reported in this paper were partially performed at TUBITAK ULAKBIM, High Performance and Grid Computing Center (TRUBA resources).

¹ David Radice, personal communication

DATA AVAILABILITY

The data generated in this article is available for a reasonable request from the corresponding author.

REFERENCES

- Abbott B. P., et al., 2017a, *Physical Review Letters*, 119, 161101
 Abbott B. P., et al., 2017b, *The Astrophysical Journal Letters*, 848, L13
 Abbott B. P., et al., 2019a, *Physical Review X*, 9, 011001
 Abbott B. P., et al., 2019b, *Physical Review Letters*, 123, 011102
 Abbott B. P., et al., 2020, *The Astrophysical Journal Letters*, 892, L3
 Acernese F., et al., 2015, *Classical and Quantum Gravity*, 32, 024001
 Allen G., Goodale T., Masso J., Seidel E., 1999, in Proceedings. The Eighth International Symposium on High Performance Distributed Computing (Cat. No.99TH8469). pp 57–61, doi:10.1109/HPDC.1999.805282, <https://ieeexplore.ieee.org/document/805282>
 Babiuc-Hamilton M., et al., 2019, *Zenodo*
 Baker T., Bellini E., Ferreira P. G., Lagos M., Noller J., Sawicki I., 2017, *Physical Review Letters*, 119, 251301
 Banyuls F., Font J. A., Ibáñez J. M., Martí J. M., Miralles J. A., 1997, *The Astrophysical Journal*, 476, 221
 Baumgarte T. W., Shapiro S. L., 1998, *Physical Review D*, 59, 024007
 Baumgarte T. W., Shapiro S. L., Shibata M., 2000, *The Astrophysical Journal*, 528, L29
 Bernuzzi S., Hilditch D., 2010, *Physical Review D*, 81, 084003
 Bernuzzi S., Dietrich T., Tichy W., Brüggmann B., 2014, *Physical Review D*, 89, 104021
 Bernuzzi S., Radice D., Ott C. D., Roberts L. F., Moesta P., Galeazzi F., 2016, *Physical Review D*, 94, 024023
 Brown J. D., Diener P., Sarbach O., Schnetter E., Tiglio M., 2009, *Phys. Rev. D*, 79, 044023
 Cactus developers 2023a, Cactus Computational Toolkit, <https://www.cactuscode.org> (accessed June 19, 2024)
 Cactus developers 2023b, Cactus Computational Toolkit Prizes, <https://www.cactuscode.org/media/prizes> (accessed June 19, 2024)
 Camilletti A., Perego A., Guercilena F. M., Bernuzzi S., Radice D., 2024, *Phys. Rev. D*, 109, 063023
 Campanelli M., Lousto C. O., Zlochower Y., 2006, *Physical Review D*, 74, 041501
 Collaboration T. L. S., et al., 2015, *Classical and Quantum Gravity*, 32, 074001
 Cutler C., Flanagan E., 1994, *Physical Review D*, 49, 2658
 Cutler C., et al., 1993, *Physical Review Letters*, 70, 2984
 Dietrich T., Bernuzzi S., Ujevic M., Tichy W., 2017a, *Phys. Rev. D*, 95, 044045
 Dietrich T., Ujevic M., Tichy W., Bernuzzi S., Brüggmann B., 2017b, *Physical Review D*, 95, 024029
 Dreyer O., Krishnan B., Shoemaker D., Schnetter E., 2003, *Phys. Rev. D*, 67, 024018
 East W. E., Paschalidis V., Pretorius F., Shapiro S. L., 2016, *Physical Review D*, 93, 024011
 East W. E., Paschalidis V., Pretorius F., Tsokaros A., 2019, *Phys. Rev. D*, 100, 124042
 Eichler D., Livio M., Piran T., Schramm D. N., 1989, *Nature*, 340, 126
 Einfeldt B., 1988, *SIAM Journal on Numerical Analysis*, 25, 294
 Etienne Z. B., Liu Y. T., Shapiro S. L., Baumgarte T. W., 2009, *Phys. Rev. D*, 79, 044024
 Evans M., Sturani R., Vitale S., Hall S., 2020, LIGO-T1500293-v13: Unofficial sensitivity curves (ASD) for aLIGO, Kagra, Virgo, Voyager, Cosmic Explorer, and Einstein Telescope, <https://dcc.ligo.org/LIGO-T1500293/public> (accessed June 19, 2024)
 Finn L. S., Chernoff D. F., 1993, *Physical Review D*, 47, 2198
 Flanagan E. E., Hinderer T., 2008, *Physical Review D*, 77, 021502
 Foucart F., 2020, *Frontiers in Astronomy and Space Sciences*, 7, 46
 Foucart F., 2023, *Living Reviews in Computational Astrophysics*, 9, 1
 Goodale T., Allen G., Lanfermann G., Massó J., Radke T., Seidel E., Shalf J.,

- 2003, in Palma J. M. L. M., Sousa A. A., Dongarra J., Hernández V., eds, High Performance Computing for Computational Science — VECPAR 2002. Lecture Notes in Computer Science. Springer, Berlin, Heidelberg, pp 197–227, doi:10.1007/3-540-36569-9_13
- Gottlieb S., Ketcheson D. I., Shu C.-W., 2009, *Journal of Scientific Computing*, 38, 251
- Grandclement P., 2010, *J. Comput. Phys.*, 229, 3334
- Hallinan G., et al., 2017, *Science*, 358, 1579
- Hilditch D., Bernuzzi S., Thierfelder M., Cao Z., Tichy W., Brüggmann B., 2013, *Physical Review D*, 88, 084057
- Hinderer T., 2008, *The Astrophysical Journal*, 677, 1216
- Hinderer T., Lackey B. D., Lang R. N., Read J. S., 2010, *Physical Review D*, 81, 123016
- Kafka P., 1988, in Burke W. R., ed., ESA Special Publication Vol. 283, ESA Special Publication. pp 121–130
- Kasen D., Badnell N. R., Barnes J., 2013, *The Astrophysical Journal*, 774, 25
- Kasen D., Metzger B., Barnes J., Quataert E., Ramirez-Ruiz E., 2017, *Nature*, 551, 80
- Kastaun W., 2021, Astrophysics Source Code Library, p. ascl:2107.017
- Kastaun W., Galeazzi F., 2015, *Physical Review D*, 91, 064027
- Kastaun W., Galeazzi F., Alic D., Rezzolla L., Font J. A., 2013, *Physical Review D*, 88, 021501
- Lattimer J. M., 2012, *Annual Review of Nuclear and Particle Science*, 62, 485
- Löffler F., et al., 2012, *Classical and Quantum Gravity*, 29, 115001
- Maggiore M., et al., 2020, *Journal of Cosmology and Astroparticle Physics*, 2020, 050
- Marronetti P., Shapiro S. L., 2003, *Physical Review D*, 68, 104024
- Nakamura T., Oohara K., Kojima Y., 1987, *Prog. Theor. Phys. Suppl.*, 90, 1
- O’Connor E., Ott C. D., 2010, *Classical and Quantum Gravity*, 27, 114103
- Papenfort L. J., Tootle S. D., Grandclement P., Most E. R., Rezzolla L., 2021, *Physical Review D*, 104, 024057
- Papenfort L. J., Most E. R., Tootle S., Rezzolla L., 2022, *Monthly Notices of the Royal Astronomical Society*, 513, 3646
- Paschalidis V., East W. E., Pretorius F., Shapiro S. L., 2015, *Physical Review D*, 92, 121502
- Pian E., et al., 2017, *Nature*, 551, 67
- Piran T., 1992, *The Astrophysical Journal*, 389, L45
- Pollney D., Reisswig C., Schnetter E., Dorband N., Diener P., 2011, *Physical Review D*, 83, 044045
- Radice D., 2020, *Symmetry*, 12, 1249
- Radice D., 2023, Scientific Data Library, <https://bitbucket.org/dradice/scidata> (accessed June 19, 2024)
- Radice D., Rezzolla L., 2012, *Astronomy and Astrophysics*, 547, A26
- Radice D., Rezzolla L., Galeazzi F., 2014a, *Classical and Quantum Gravity*, 31, 075012
- Radice D., Rezzolla L., Galeazzi F., 2014b, *Monthly Notices of the Royal Astronomical Society*, 437, L46
- Radice D., Rezzolla L., Galeazzi F., 2015, in Pogorelov N. V., Audit E., Zank G. P., eds, Astronomical Society of the Pacific Conference Series Vol. 498, Numerical Modeling of Space Plasma Flows ASTRONUM-2014. p. 121 (arXiv:1502.00551), doi:10.48550/arXiv.1502.00551
- Radice D., Bernuzzi S., Ott C. D., 2016a, *Physical Review D*, 94, 064011
- Radice D., Galeazzi F., Lippuner J., Roberts L. F., Ott C. D., Rezzolla L., 2016b, *Monthly Notices of the Royal Astronomical Society*, 460, 3255
- Radice D., Perego A., Hotokezaka K., Fromm S. A., Bernuzzi S., Roberts L. F., 2018, *The Astrophysical Journal*, 869, 130
- Read J. S., Markakis C., Shibata M., Uryū K., Creighton J. D. E., Friedman J. L., 2009, *Physical Review D*, 79, 124033
- Read J. S., et al., 2013, *Physical Review D*, 88, 044042
- Reisswig C., Pollney D., 2011, *Classical and Quantum Gravity*, 28, 195015
- Rosswog S., Torsello F., Diener P., 2023, *Frontiers in Applied Mathematics and Statistics*, 9
- Rosswog S., Diener P., Torsello F., Tauris T. M., Sarin N., 2024, *Monthly Notices of the Royal Astronomical Society*, 530, 2336
- Ruffert M., Janka H. T., 2001, *Astronomy and Astrophysics*, 380, 544
- Ruffert M., Janka H. T., Schäfer G., 1995, *Astrophysics and Space Science*, 231, 423
- Ruffert M., Janka H. T., Takahashi K., Schaefer G., 1997, *Astronomy and Astrophysics*, 319, 122
- Sakstein J., Jain B., 2017, *Physical Review Letters*, 119, 251303
- Schianchi F., Ujevic M., Neuweiler A., Gieg H., Markin I., Dietrich T., 2024, Black-hole formation in binary neutron star mergers: The impact of spin on the prompt-collapse scenario (arXiv:2402.16626)
- Schnetter E., Hawley S. H., Hawke I., 2004, *Classical and Quantum Gravity*, 21, 1465
- Shibata M., Nakamura T., 1995, *Physical Review D*, 52, 5428
- Shibata M., Taniguchi K., Uryū K. b. o., 2005, *Phys. Rev. D*, 71, 084021
- Smartt S. J., et al., 2017, *Nature*, 551, 75
- Steiner A. W., Hempel M., Fischer T., 2013, *The Astrophysical Journal*, 774, 17
- Stellarcollapse 2017, stellarcollapse.org, <https://stellarcollapse.org> (accessed June 19, 2024)
- Suresh A., Huynh H. T., 1997, *Journal of Computational Physics*, 136, 83
- Tacik N., et al., 2015, *Physical Review D*, 92, 124012
- The Einstein Toolkit 2024, The Einstein Toolkit, <https://einstein toolkit.org> (accessed June 19, 2024)
- The LIGO Scientific Collaboration 2015, *Classical and Quantum Gravity*, 32, 074001
- The LIGO Scientific Collaboration and the Virgo Collaboration et al., 2018, *Physical Review Letters*, 121, 161101
- Thornburg J., 1996, *Physical Review D*, 54, 4899
- Thornburg J., 2004, *Classical and Quantum Gravity*, 21, 743
- Tichy W., 2006, *Physical Review D*, 74, 084005
- Tichy W., 2009a, *Classical and Quantum Gravity*, 26, 175018
- Tichy W., 2009b, *Physical Review D*, 80, 104034
- Tichy W., 2011, *Physical Review D*, 84, 024041
- Tichy W., 2012, *Physical Review D*, 86, 064024
- Tichy W., Rashti A., Dietrich T., Dudi R., Brüggmann B., 2019, *Physical Review D*, 100, 124046
- Troja E., et al., 2017, *Nature*, 551, 71
- Tsatsin P., Marronetti P., 2013, *Physical Review D*, 88, 064060
- Weyhausen A., Bernuzzi S., Hilditch D., 2012, *Physical Review D*, 85, 024038
- Wilson J. R., Mathews G. J., 1995, *Physical Review Letters*, 75, 4161
- Zilhão M., Löffler F., 2013, *International Journal of Modern Physics A*, 28, 1340014
- Zlochower Y., et al., 2022, *Zenodo*

APPENDIX A: APPENDIX

In this section, we provide average energy and peak neutrino luminosities for all flavours in Table A1 and in Table A2. We also provide the energy and angular momentum release due to gravitational radiation in Table A3 and in Table A4.

This paper has been typeset from a $\text{\TeX}/\text{\LaTeX}$ file prepared by the author.

Table A1. The average neutrino energy, $\langle E_\nu \rangle$. The electron neutrino, electron anti-neutrino and heavy-lepton neutrinos are represented with ν_e , $\bar{\nu}_e$ and ν_μ , respectively. The values given with \pm show the difference between two resolutions.

Model	$\langle E_\nu \rangle$ (MeV)					
	ν_e		$\bar{\nu}_e$		ν_μ	
	$t_{dyn,1}$	$t_{dyn,2}$	$t_{dyn,1}$	$t_{dyn,2}$	$t_{dyn,1}$	$t_{dyn,2}$
$\chi = 0[1]$	13.16 ± 0.20	–	17.56 ± 0.18	–	23.18 ± 0.52	–
$\chi = -0.2$	13.74 ± 0.24	13.54 ± 0.18	17.79 ± 0.17	18.42 ± 0.28	24.49 ± 0.34	26.67 ± 0.27
$\chi = 0.2$	12.34 ± 0.23	–	16.91 ± 0.21	–	23.32 ± 0.13	–
$\chi = -0.4$	15.07 ± 0.15	16.54 ± 0.42	18.86 ± 0.13	20.93 ± 0.14	25.93 ± 0.48	28.60 ± 0.53
$\chi = 0[2]$	12.71 ± 0.25	13.03 ± 0.13	16.97 ± 0.54	17.80 ± 0.74	23.33 ± 0.16	25.10 ± 0.37
$\chi = 0.4$	11.73 ± 0.55	12.25 ± 0.34	15.75 ± 0.61	15.77 ± 0.63	23.44 ± 0.14	24.39 ± 0.10
$\chi = -0.65$	15.02 ± 0.39	16.75 ± 0.36	20.13 ± 0.70	22.01 ± 0.55	28.41 ± 0.35	31.44 ± 0.08
$\chi = 0[3]$	0.00	0.00	0.00	0.00	0.00	0.00
$\chi = 0.67$	12.55 ± 0.29	13.11 ± 0.45	16.11 ± 0.39	16.61 ± 0.44	23.42 ± 0.01	24.39 ± 0.04
$305q1\chi0$	7.28	–	8.83	–	9.71	–
$305q1\chi0.4$	12.43	9.42	16.92	12.03	22.71	15.14
$305q205\chi0$	11.47	–	13.60	–	16.18	–
$305q205\chi0.4$	13.48	0.00	17.20	0.00	23.49	0.00
$41q1\chi0[1]$	3.18	–	3.19	–	2.44	–
$41q1\chi0[2]$	4.50	–	5.06	–	4.41	–
$41q1\chi - 0.65$	0.54	–	0.56	–	0.67	–
$41q1\chi0.67$	6.40	–	7.36	–	7.40	–

Table A2. The peak neutrino luminosities, L_ν^{peak} for electron neutrinos, electron anti-neutrinos and heavy-lepton neutrinos which are represented with ν_e , $\bar{\nu}_e$ and ν_μ , respectively. The values given with \pm show the difference between two resolutions.

Model	L_ν^{peak} ($\times 10^{52}$ ergs $^{-1}$)		
	ν_e	$\bar{\nu}_e$	ν_μ
$\chi = 0[1]$	0.57 ± 0.26	1.75 ± 0.85	2.71 ± 0.99
$\chi = -0.2$	0.72 ± 0.34	2.32 ± 1.43	3.78 ± 1.81
$\chi = 0.2$	0.32 ± 0.11	2.07 ± 1.63	1.34 ± 0.47
$\chi = -0.4$	1.05 ± 0.71	2.68 ± 0.74	4.43 ± 1.30
$\chi = 0[2]$	0.59 ± 0.29	1.48 ± 0.36	2.34 ± 0.64
$\chi = 0.4$	1.78 ± 1.15	3.89 ± 3.24	0.69 ± 0.37
$\chi = -0.65$	0.48 ± 0.10	4.21 ± 2.71	2.90 ± 0.22
$\chi = 0[3]$	0.31 ± 0.09	2.85 ± 2.01	3.33 ± 1.30
$\chi = 0.67$	0.34 ± 0.19	0.74 ± 0.34	0.37 ± 0.15
$305q1\chi0$	0.96	2.51	4.99
$305q1\chi0.4$	0.12	0.39	1.22
$305q205\chi0$	2.96	34.40	22.10
$305q205\chi0.4$	1.41	2.86	7.92
$41q1\chi0[1]$	1.59	26.30	7.46
$41q1\chi0[2]$	0.98	16.40	6.56
$41q1\chi - 0.65$	0.63	1.72	2.56
$41q1\chi0.67$	2.30	33.30	10.30

Table A3. Energy radiated by gravitational waves. E_{ins}^{gw} , E_{tot}^{gw} and E_{tot}^{gw}/M_{tot} show energy loss during inspiral, the total energy loss and the ratio of the total energy loss to the total initial mass energy, respectively. The values given with \pm show the difference between two resolutions.

Model	E_{ins}^{gw} (%)		E_{tot}^{gw} ($\times 10^{52}$ ergs)		E_{tot}^{gw}/M_{tot} ($\times 10^{-2}$)	
	$t_{dyn,1}$	$t_{dyn,2}$	$t_{dyn,1}$	$t_{dyn,2}$	$t_{dyn,1}$	$t_{dyn,2}$
$\chi = 0[1]$	24 ± 4.52	-	6.85 ± 0.42	-	1.51 ± 0.09	-
$\chi = -0.2$	13 ± 0.94	9.64 ± 2.06	4.67 ± 0.38	6.25 ± 1.18	1.03 ± 0.08	1.37 ± 0.26
$\chi = 0.2$	51 ± 15.05	-	5.51 ± 0.08	-	1.21 ± 0.02	-
$\chi = -0.4$	16 ± 4.02	12.76 ± 2.24	2.59 ± 0.80	3.26 ± 0.62	0.57 ± 0.18	0.72 ± 0.14
$\chi = 0[2]$	39 ± 15.61	33.28 ± 18.29	3.24 ± 0.95	3.75 ± 1.34	0.71 ± 0.21	0.82 ± 0.30
$\chi = 0.4$	40 ± 11.17	32.32 ± 9.52	5.48 ± 0.37	6.84 ± 0.55	1.20 ± 0.08	1.50 ± 0.12
$\chi = -0.65$	65 ± 1.11	62.58 ± 0.14	4.00 ± 0.14	4.14 ± 0.08	0.88 ± 0.03	0.91 ± 0.02
$\chi = 0[3]$	64 ± 5.07	63.32 ± 4.45	2.31 ± 0.13	2.33 ± 0.12	0.51 ± 0.03	0.51 ± 0.03
$\chi = 0.67$	76 ± 23.21	68.18 ± 21.90	3.12 ± 0.10	3.45 ± 0.04	0.68 ± 0.02	0.76 ± 0.01
305q1 χ 0	53.55	-	4.71	-	0.86	-
305q1 χ 0.4	26.33	24.56	11.48	12.32	2.11	2.26
305q205 χ 0	68.56	-	2.23	-	0.41	-
305q205 χ 0.4	64.06	60.09	2.56	2.73	0.47	0.50
41q1 χ 0[1]	40.17	-	10.95	-	1.49	-
41q1 χ 0[2]	62.79	-	11.16	-	1.52	-
41q1 $\chi - 0.65$	61.36	-	8.70	-	1.19	-
41q1 χ 0.67	47.96	-	13.12	-	1.79	-

Table A4. Angular momentum radiated by gravitational waves. The J_{ins}^{gw} , J_{tot}^{gw} and J_{tot}^{gw}/J_0 show angular momentum loss during the inspiral, the total angular momentum loss and the ratio of the total angular momentum loss to the total initial angular momentum, respectively. The values given with \pm show the difference between two resolutions.

Model	J_{ins}^{gw} (%)		J_{tot}^{gw} (M_{\odot}^2)		J_{tot}^{gw}/J_0 ($\times 10^{-2}$)	
	$t_{dyn,1}$	$t_{dyn,2}$	$t_{dyn,1}$	$t_{dyn,2}$	$t_{dyn,1}$	$t_{dyn,2}$
$\chi = 0[1]$	47 ± 5.10	-	1.36 ± 0.08	-	22 ± 1.24	-
$\chi = -0.2$	28 ± 1.83	22 ± 3.86	0.83 ± 0.06	1.04 ± 0.16	14 ± 1.00	18 ± 2.80
$\chi = 0.2$	70 ± 12.20	-	1.26 ± 0.02	-	18 ± 0.29	-
$\chi = -0.4$	32 ± 6.84	27 ± 4.32	0.48 ± 0.13	0.57 ± 0.19	9 ± 2.42	11 ± 2.00
$\chi = 0[2]$	58 ± 13.52	52 ± 17.02	0.66 ± 0.14	0.73 ± 0.19	10 ± 2.16	11 ± 3.00
$\chi = 0.4$	62 ± 9.31	54 ± 8.69	1.31 ± 0.08	1.49 ± 0.11	17 ± 1.10	20 ± 1.38
$\chi = -0.65$	76 ± 0.43	75 ± 0.38	0.83 ± 0.02	0.86 ± 0.02	19 ± 0.53	19 ± 0.34
$\chi = 0[3]$	76 ± 3.46	75 ± 3.12	0.70 ± 0.03	0.71 ± 0.03	11 ± 0.48	11 ± 0.44
$\chi = 0.67$	87 ± 18.09	83 ± 17.90	0.89 ± 0.03	0.93 ± 0.03	11 ± 0.41	11 ± 0.33
305q1 χ 0	71.04	-	1.26	-	14.50	-
305q1 χ 0.4	48.66	46.89	2.14	2.22	20.71	21.49
305q205 χ 0	77.10	-	0.74	-	9.72	-
305q205 χ 0.4	76.28	74.55	0.83	0.85	8.30	8.50
41q1 χ 0[1]	59.03	-	1.98	-	13.71	-
41q1 χ 0[2]	75.49	-	2.30	-	15.94	-
41q1 $\chi - 0.65$	75.24	-	1.61	-	16.55	-
41q1 χ 0.67	62.59	-	3.02	-	15.70	-